UNIVERSIDADE DE LISBOA
FACULDADE DE CIÊNCIAS
DEPARTAMENTO DE FÍSICA

Simulation of Auger Electron Spectra from Nuclides of Medical Interest

Maria Daniela Salvado Pires

Mestrado em Física
Especialização em Física Nuclear e Partículas

Dissertação orientada por:
Professor Doutor José Pires Marques
Professor Doutor Jorge Miguel Sampaio

2020

To the memory of my father, my one and only Master.
To my mother, always.

Acknowledgments

This has been a long journey, so I would like to start thanking to my supervisors. Firstly, my supervisor José Pires Marques for his wisdom, patience and guidance, and for transmitting me so much enthusiasm through the completion of this work; Jorge Sampaio for his essencial insights and patience to teach me and help me. You are both a source of inspiration.

I would like to mention my good friends Marco Pinto, Bruno Agatão and Sandra Brás for their support, patience and friendship, always. I am also very grateful to the friends I made during my time at FCUL, João Pereira and João Especial.

Finally, I am truly grateful to my parents and my brother for their love, encouragement and support. You always showed me the way.

Resumo

O efeito de Auger foi primeiramente observado e interpretado por Pierre Auger, nos anos 1923-25, que o descreveu como sendo a emissão de um eletrão como resultado de um processo de reabsorção interna que se seguiria à ionização inicial de um átomo. Dois anos depois, Gregor Wentzel apresentou a sua teoria não-relativista para o mesmo efeito, explicando-o como uma autoionização e um processo de relaxação atómicos como consequência da ionização de uma camada interna. Esta ionização poderá ocorrer por fotoionização, impacto de partículas carregadas, ou como resultado de processos de decaimento nuclear como são a captura eletrónica e a conversão interna.

Um átomo que sofre uma captura eletrónica ou conversão interna emite, tipicamente, eletrões com energias de até $\sim$100 eV, o que implica que tenham alcances muito curtos, da ordem dos nanómetros ou micrómetros, depositando toda a sua energia numa vizinhança próxima do átomo em que tiveram origem. Esta característica torna os radionuclídeos emissores de Auger adequados para terapias de tratamento de câncro, permitindo a poupança dos tecidos adjacentes ao tumor a tratar. São diversos os mecanismos que induzem morte celular tumoral por ação de radiação, divididos essencialmente em ionização direta ou indireta das moléculas do DNA; no caso dos eletrões de Auger, o seu efeito é, essencialmente, a fragmentação dupla e/ou única da cadeia de DNA, cujos efeito serão dificilmente colmatáveis pelos mecanismos celulares próprios de reparação. Os danos adjacentes provocados pelas ionizações induzidas por radiação dependem das partículas envolvidas e da energia depositada, mas são habitualmente parametrizados através da *Tranferência Linear de Energia*, que representa a energia depositada por unidade de comprimento do percurso atravessado. Para os eletrões Auger esta transferência é significativa: apesar das suas baixas energias, os seus curtos alcances permitem atingir valores elevados. Contudo, para determinar de forma precisa a eficácia biológica destes radionuclídeos é necessário o conhecimento do respetivo espectro de emissão, o que requer a determinação detalhada das correspondentes probabilidades e energias de transição atómicas e a simulação da cascata de lacunas que é gerada a partir da ionização atómica inicial. Tratando-se de um processo estocástico, a cascata característica do processo de relaxação atómica pode ser bem descrita através de métodos Monte Carlo. Os diversos passos da simulação desta cascata correspondem, de uma forma sucinta, primeiramente à distribuição dos eletrões pelas camadas e subcamadas atómicas de acordo com a configuração do átomo neutro; em seguida a seleção aleatória da camada em que é criada uma lacuna, de acordo com as suas probabilidades correspondentes. À seleção da camada em que é gerada a lacuna segue-se a da transição, radiativa ou de Auger, que também é feita através de um gerador de números aleatórios e de acordo com as probabilidades de transição e energias correspondentes calculadas. O processo repete-se até que sejam atingidas as subcamadas mais externas ou que não existam mais possibilidades para que transiçoes aconteçam.

A base de dados atómicos *Evaluated Atomic Data Library, EADL* apresenta tabelas das probabilidades de transições atómicas calculadas para sistemas ionizados com uma lacuna. Contudo o método de cálculo, nomeadamente o método de Dirac-Hartree-Slater, não reflete o estado da arte, uma vez que exclui a correlação eletrónica. Uma vez que cálculos baseados no método multiconfiguracional de Dirac-Fock permitem a inclusão de efeitos e correções rel-

ativistas na determinação das funções de estado das configurações atómicas, a sua utilização permite melhorias e precisão significativas nos cálculos de estrutura e propriedades atómicas. A par com essa característica, a atualização dos dados das tabelas da EADL permite também a inclusão dos valores de probabilidades e energias de transição para camadas mais externas N e O, uma vez que os valores disponíveis até então têm como limite a camada M.

Com as atuais bases de dados de probabilidades de transição e rendimentos radiativos e de Auger a necessitarem de atualização, a Agência Internacional de Energia Atómica lançou um apelo para um projeto de investigação com o objetivo de determinar aqueles valores de forma mais precisa. Deste modo, este trabalho apresenta probabilidades de transições atómicas, e respetivas energias, atualizadas, e determinados através da implementação do Método de Dirac-Fock através do código MCDFGME para o elemento ^{125}I, considerando diferentes configurações eletrónicas com o mesmo valor de J, obtidas a partir dos diferentes acoplamentos jj possíveis. Seguidamente, os resultados da simulação de Monte Carlo da cascata característica do processo de relaxação atómica e respectivos espectros de Auger também são apresentados.

A escolha do elemento ^{125}I para este trabalho prende-se com o fato de, além de ser emissor de eletrões de Auger, ser já commumente utilizado em tratamentos de Braquiterapia prostática de baixa taxa de dose devido ao seu valor de meia-vida de aproximadamente 60 dias: nem tão baixo que não permita uma gestão razoável do tempo de tratamento, nem demasiado elevado, do ponto de vista clínico, que provoque danos adjacentes ao tratamento para o paciente até que decaia, sem riscos, para o elemento estável ^{125}Te.

Para estudar o impacto das diferenças, a uma escala microdosimétrica, entre os dados do Arquivo de Dados Atómicos Avaliados e os valores calculados com o código MCDFGME, o espetro de Auger simulado para o ^{125}Te foi usado para simular o processo de deposição de energia, pelos eletrões de Auger, num modelo celular virtual, usando o código de simulação de transporte de partículas PENELOPE. Devido ao seu curto alcance, da ordem das escalas nano- e micrométricas, a microdosimetria dos eletrões de Auger é habitualmente estudada com recurso a simulações Monte Carlo em comparação com métodos semi-analíticos como o são o *Medical Internal Radiation Dose, MIRD*, frequentemente utilizado como referência para validação de métodos estocásticos para estudos de microdosimetria. Com efeito, foram simuladas as deposições de energia por eletrões de Auger em duas geometrias celulares: a primeira constituída por citoplasma, núcleo e um cromossoma contendo a fonte pontual e isotrópica de ^{125}I; a segunda contendo citoplasma, núcleo e 6 cromossomas. Para esta segunda geometria foram realizadas simulações com a fonte de ^{125}I colocada num cromossoma centrado com a célula e com a mesma fonte colocada num cromossoma mais afastado do centro. Para as duas geometrias as simulações foram feitas com os espetros derivados dos dados EADL e os espetros obtidos através dos cálculos realizados com o código MCDFGME. Os resultados são apresentados e discutidos de forma a perceber o impacto das atualizações dos dados de estrutura atómica proporcionadas pela utilização do Método de Dirac-Fock.

Finalmente, no seguimento das conclusões sobre a os resultados apresentados e sua discussão, são apresentadas algumas perspectivas para trabalhos futuros, que se poderão traduzir em estudos mais aprofundados e melhorias mais ou menos significativas da precisão dos cálculos efetuados. Um dos aspetos referidos está essencialmente relacionado com a in-

clusão dos efeitos de *shake-off* e de *shake-up* que podem ocorrer depois da ionização por um processo de fotoionização, Captura Eletrónica ou Conversão Interna, e que podem alterar significativamente o potencial central do átomo e conduzir a diferentes resultados de probabilidades e energias de transição. O segundo aspeto apresentado relaciona-se com o facto das simulações com o código PENELOPE terem um limite inferior de 50 eV no transporte de eletrões, o que é insuficiente para descrever os a deposição dos eletrões de Auger emitidos nas transições das camadas mais externas.

Palavras-chave: Auger, eletrões, Arquivo de Dados Atómicos Avaliados, Método Dirac-Fock, Monte Carlo

Abstract

The Auger effect was first observed and interpreted by Pierre Auger back in the years 1923-25 as the emission of an electron resulting from an internal reabsorption process that follows an initial internal ionization of an atom. Two years after, Gregor Wentzel presented a non-relativistic theory for the same effect, explaining it as an autoionization and atomic relaxation process, in consequence of a single ionization in an inner atomic shell. The ionization may occur by photoionization, by impact of charged particles, or as a consequence of nuclear decays like electron capture and internal conversion.

An atom that undergoes an electron capture or internal conversion typically emits electrons with energies in the range of a few up to $\sim$100 eV, which implies they have short ranges, from nanometers to micrometers, so the Auger electrons may deposit all energy in their near vicinity. This feature makes the radionuclides that are Auger emitters suitable to cancer therapy, sparing normal tissues adjacent to the tumor. To accurately determine the biological effciency of these radionuclides, it is necessary the knowledge of their emission spectra, which implies the accurate determination of atomic transition energies and probabilities, and the simulation of the vacancy cascade of the atomic relaxation process. Being a stochastic process, the characteristic cascade of that atomic relaxation can be well described using a Monte Carlo approach.

The *Evaluated Atomic Data Library* (EADL) tabulates atomic transition probabilities calculated for the singly-ionized systems. The approach used for the determination of those data, namely the Dirac-Hartree-Slater method, does not reflect the state-of-the art and limit the accuracy of the resulting X-ray and Auger spectra, since it excludes, for example, electronic correlation. Since methods like Multiconfiguration Dirac-Fock Method take relativistic effects and electronic correlation into account in solving configuration state functions, it allow significant improvements on the calculations of atomic properties.

With the current database of radiative and Auger transition probabilities and yields outdated, the International Atomic Energy Agency called for a coordinate research project with the aim of determining those values more accurately, therefore this thesis presents the udpated atomic transition probabilities and energies determined using the Dirac-Fock method implemented with the MCDFGME code, the results for the simulation of the atomic relaxation cascade with a Monte Carlo program and the generated Auger electron spectra. To infer on the impact of the differences between the updated data and the EADL database at a microdosimetric scale, the simulated ^{125}I Auger spectrum was used to simulate the energy deposited in a simple cell model, using the Monte Carlo particle transport code PENELOPE.

Keywords: Auger, electrons, Evaluated Atomic Data Library, Dirac-Fock Method, Monte Carlo

Contents

Acknowledgments . . . v

Resumo . . . vii

Abstract . . . xi

List of Tables . . . xvii

List of Figures . . . xix

1 Introduction 1

1.1 Auger-Electron Radionuclide Therapy . . . 3

1.1.1 Iodine-125 . . . 6

1.2 Objectives . . . 6

1.3 Thesis Outline . . . 7

2 Calculation of Atomic transitions 9

2.1 Relativistic Calculation of Atomic Properties . . . 9

2.1.1 Dirac-Fock Method . . . 10

2.1.2 Relativistic Hamiltonian of the System . . . 12

2.2 Calculation of atomic transitions . . . 13

2.2.1 Radiative Transitions . . . 13

2.2.2 Auger Transitions . . . 14

3 Calculation of atomic fundamental parameters 16

3.1 Inner-shell vacancy production . . . 16

3.1.1 Electron Capture . . . 16

3.1.2 Internal Conversion . . . 17

3.1.3 Number of inner-shell vacancies created . . . 17

3.2 Atomic Relaxation . . . 18

3.2.1 Fundamental atomic parameters 19
3.2.2 EADL type formats 20
3.3 Monte Carlo Simulation of Auger-electron Spectra 20
3.3.1 Shake-off and Shake-up 22

4 Atomic transition probabilities and yields for argon-40 and tellurium-125 25

4.1 Atomic Transitions of ^{40}Ar 25
4.1.1 Auger Transition Probabilities 26
4.1.2 Radiative Transition Probabilities 26
4.1.3 Atomic Shell Widths 28
4.1.4 Auger Yields 29
4.1.5 Radiative Yields 30
4.2 Atomic Transitions of ^{125}Te 31
4.2.1 Auger Normalized Transition Probabilities 31
4.2.2 Radiative Transition Probabilities 33
4.2.3 Atomic shell widths 35
4.2.4 Auger Yields 36
4.2.5 Radiative Yields 36
4.3 Monte Carlo Simulation of Auger Electron Spectra 39

5 Microdosimetric simulations 41

5.1 MIRD model using PENELOPE 41
5.2 Results for ^{125}I microdosimetric calculations 43
5.2.1 S-values for MIRD geometry: MCDFGME and EADL data 43
5.2.2 S-values for modified MIRD geometry: MCDFGME and EADL data 44
5.2.3 Radial Dose distribution: MCDFGME and EADL data 45
5.2.4 Auger energy deposition spectra: MCDFGME and EADL data 46
5.2.5 Linear Energy Transfer: MCDFGME and EADL data 47

6 Conclusions 49

6.1 Prospects for future work 51
6.1.1 Calculations of atomic parameters 51
6.1.2 Microdosimetric simulations 51

Bibliography **53**

List of Tables

3.1 Subshell correspondence to IUPAC notation 19

4.1 Radiative (R) and Auger (NR) sububshell widths for ^{40}Ar in eV. 29

4.2 Subshell Auger yields for ^{40}Ar. 30

4.3 Shell Auger yields for ^{40}Ar. 30

4.4 Subshell fluorescence yields for ^{40}Ar. 30

4.5 ^{40}Ar: Fluorescence yields for K and L shells 30

4.6 ^{125}Te: Shell widths for K, L$_{1-3}$, M$_{1-5}$, N$_{1-5}$ and O$_{1-3}$ subshells 35

4.7 ^{125}Te: Auger yields for K, L$_{1-3}$, M$_{1-5}$ and N$_{1-5}$ subshells 36

4.8 ^{125}Te: Auger yields ω_i for K, L, M and N shells 36

4.9 ^{125}Te: Fluorescence yields for K, L$_{1-3}$, M$_{1-5}$, and N$_{1-5}$ subshells 37

4.10 ^{125}Te: Fluorescence yields for K, L, M and N shells 38

5.1 S-values for simple MIRD geometry considered: 1 cell with the source positioned at the center of the chromosome 44

5.2 Comparison of S-values for MIRD geometry considered 44

5.3 S-values for modified MIRD geometry considered: 6 chromosomes with the source positioned at the center of the nucleus 45

5.4 S-values for modified MIRD geometry considered: 6 chromosomes with the source positioned at the center of the nucleus 45

List of Figures

1.1 Typical set of tracks observed by Pierre Auger 2

1.2 Illustration of the track of α, β particles and Auger electrons emitted by radiolabeled monoclonal antibodies targeted to cancer cells. 4

1.3 Linear energy transfer (LET) along paths of energetic beta particles and Auger electrons as function of traversed distance. 4

1.4 Mammalian cell survival curves after low and high LET irradiation. 5

1.5 ^{125}I decay scheme 6

2.1 Feynman diagram for the first-order Lamb shift of a bound electronic state: vacuum polarization 13

2.2 Feynman diagram for the first-order Lamb shift of a bound electronic state: self-energy 14

3.1 Illustration of radiative and non-radiative transitions. 18

3.2 Cascade illustration of Auger transitions following excitation of an atom A. 21

4.1 Normalized Auger transition probabilities, f^{NR}_{MCDFGME}, for ^{40}Ar as a function of MCDFGME average transition energies $\bar{E}_{XY}$ in eV. 26

4.2 Ratio of the normalized Auger transition probabilities, $f^{NR}_{\text{MCDFGME}}/f^{NR}_{\text{EADL}}$, for ^{40}Ar as a function of MCDFGME average transition energies $\bar{E}_{XY}$ in eV. 27

4.3 Ratio of the normalized Auger transition probabilities, $f^{NR}_{\text{MCDFGME}}/f^{NR}_{\text{EADL}}$, for ^{40}Ar as a function of MCDFGME average normalized transition probabilities f^{NR}_{MCDFGME}. 27

4.4 Normalized radiative transition probabilities, f^{R}_{MCDFGME}, for ^{40}Ar as a function of MCDFGME average transition energies $\bar{E}_{XY}$ in eV. 28

4.5 Ratio of the normalized radiative transition probabilities, $f^{R}_{\text{MCDFGME}}/f^{R}_{\text{EADL}}$, for ^{40}Ar as a function of MCDFGME average transition energies $\bar{E}_{XY}$ in eV. 28

4.6 Ratio of the radiative transition probabilities, $f^{NR}_{\text{MCDFGME}}/f^{NR}_{\text{EADL}}$, for ^{40}Ar as a function of MCDFGME average transition probability f^{R}_{MCDFGME}. 29

4.7 ^{125}Te: Auger normalized transition rates $f^{NR}_{MCDFGME}$ as a function of MCDFGME transition energies E_{XY} 31

4.8 ^{125}Te: Comparison of Auger normalized transition probabilities as a function of MCDFGME transition energies E_{XY} 32

4.9 ^{125}Te: Comparison of radiationless transition rates as a function of MCDFGME transition probabilities f^{NR}_{ij} 32

4.10 ^{125}Te: Radiative normalized transition probabilities as a function of MCDFGME transition energies E_{XY} 33

4.11 [^{125}Te: Comparison of radiative normalized transition probabilities as a function of MCDFGME transition energies E_{ij} 34

4.12 ^{125}Te: Comparison of radiative normalized transition probabilities as a function of MCDFGME transition probabilities f^{NR}_{ij} 34

4.13 Auger spectra obtained for EADL and MCDFGME code calculated data 39

4.14 Ratio between Auger spectra obtained for EADL and MCDFGME code calculated data 40

5.1 First virtual cell: MIRD geometry (modified) used for MC simulation 42

5.2 Second virtual cell: MIRD geometry (modified) used for MC simulation 43

5.3 ^{125}Te: radial distribution of S-values for the Auger emission (MCDFGME and EADL data) 46

5.4 ^{125}Te: Auger energy deposition spectra per decay (MCDFGME and EADL data) . 47

5.5 ^{125}Te: LET per decay for the Auger emission (MCDFGME and EADL data) 47

5.6 ^{125}Te: MCDFGME/EADL LET per decay ratio for the Auger emission 48

Chapter 1

Introduction

> Lors du départ du premier électron, sous forme du rayon β secondaire, une place est laissée libre dans le système électronique de l'atome excité. La chute d'un électron plus périphérique sur ce niveau sáccompagne de l'émission d'un quantum de rayonnement caractéristique. Ce quantum peut être absorbé dans l'atome même, et servir à la production, aux dépends des niveaux périphériques, d'un rayon β tertiaire [a].
>
> ---
>
> [a] When the first electron leaves as a secondary β-ray, there is a vacancy left in the electronic system of the excited atom. The drop of a more peripheral electron on that level is accompanied by the emission of a characteristic radiation quantum. This quantum may be absorbed in the atom itself and produce, at the expense of the peripheral levels, a tertiary β-ray.
>
> Pierre Auger

Following the first empirical demonstration of the photoelectric effect by Heinrich Hertz in 1887, X-ray photoelectron spectroscopy developed rapidly and, in the early 1920s, the photoelectron spectra of several elements had already been determined. At that time, magnetic analysis and photographic detection were used to carry out most of the experiments on the photoelectric effect, but in 1912 Charles Thomson Wilson had proposed the cloud chamber experimental setting, which allowed direct observation of the photoelectron trajectories and became known as Wilson cloud-chamber. In the years 1923-25 the french physicist Pierre Auger observed paired electron tracks emanating from atoms of inert gases (on a mixture of 95% hydrogen and 5% argon), contained in a Wilson cloud-chamber, undergoing inner shell electron transitions after exposure to 40 keV X-rays. One of the tracks corresponded represented the photoelectron; the secondary track was explained by Pierre Auger as being the result of some kind of internal conversion of potential energy into mechanical energy instead of producing an electromagnetic quantum [1].

This new effect, now known as *Auger effect* was first interpreted by Pierre Auger as representing an internal reabsorption following an initial ionization and leading to the emission of a second electron. Furthermore, if the final state had a vacancy in a core-level, the same process could give rise to a third emission:

Figure 1.1: Typical set of tracks observed by Pierre Auger. Photoelectron (long tracks) and additional electrons resulting from the action of 40 keV on an atmosphere of humid hydrogen (95%) mixed with argon (5%). [1]

> La répétition du même processus doit aboutir à la production d'un rayon quaternaire; et je crois en effet avoir observé de tels rayons dans le cas de l'iode. [a]
>
> ---
>
> [a] The repetition of that process must lead to the production of a fourth order ray; and I indeed believe I have observed such rays in the case of [gaseous] iodine.
>
> Pierre Auger

In 1927, Gregor Wentzel presented a non-relativistic theory for the Auger effect, proposing it as an autoionization process resulting from the electrostatic interaction between two electrons and following a single ionization in an inner shell. The emission of Auger electrons and characteristic X-rays constitutes an *atomic relaxation* process, which is a way for the excited atom to release its energy. The ionization may occur by irradiation of the atom with photons (photoionization) and the impact of charged particles, or as a consequence of nuclear decay modes like *Electron Capture* (EC), which corresponds to the absorption of an atomic electron by the nucleus and the emission of a neutrino and *Internal Conversion* (IC) - in which the nuclear de-excitation occurs with the emission of a γ-ray or the ejection of an atomic electron.

An atom that undergoes IC or EC typically emits electrons with energies of a few eV up to $\sim$100 eV and in a short range from nanometers to micrometers, leading to a high energy deposition in their near vicinity. This makes Auger emitters radionuclides suitable to cancer therapy, sparing normal tissues adjacent to the tumor. Every Auger electron emission produces two new vacancies whereas X-ray emission produces one vacancy. After the creation of an initial vacancy through a nuclear decay, photoionization or charged particle impact, a vacancy cascade begins and it will continue until the fulfillment of all vacancies is achieved by emissions of radiative and non-radiative transitions, or until no more atomic transitions are energetically allowed. A dosimetric evaluation of Auger-emitting radioisotopes implies knowledge on emission spectra, so transition probabilities and electron and X-ray energies must be determined with accuracy and the vacancy cascade simulated. Since Auger and X-ray transitions during the atomic relaxation are stochastic processes, the cascade process can be well described using a Monte Carlo approach.

The *Evaluated Atomic Data Library* (EADL) tabulates atomic transition probabilities [2] calculated for the singly-ionized systems in the form of branching ratios from Scofield [3, 4, 5] publications for radiative transitions and Chen et. al works on non-radiative transitions [6, 7, 8, 9, 10]. Notwithstanding, some contents and assumptions for EADL values do not reflect the state-of-the-art and limit the accuracy of the resulting spectra [11]:

- Current version of EADL tables do not include weak transitions between some outer atomic subshells;
- Transition probabilities values available in EADL database were calculated with the assumption that the (sub-)shell from which the electron will be removed is filled with the total number of electrons it can carry;
- Shake-off and shake-up[1] probabilities are not included in EADL tables;
- Dirac-Fock calculations are more accurate than Dirac-Hartree-Slater (DHS) method used to perform EADL database calculations [12], since the latter assumes the Independent Particle Model (IPM), for which electronic correlation is not included.

Several works have demonstrated that relativistic effects may alter many atomic and molecular properties [13] and calculations performed by Jean-Paul Desclaux [14] and Paul Indelicato [15, 16] have demonstrated the general agreement with experimental transition energies is very good. Methods like Multiconfiguration Dirac-Fock Method (MCDF), the relativistic equivalent of Multiconfiguration Hartree-Fock Method (MCHF), allow significant improvements on calculations of atomic properties. In this way, and since the current database of radiative and non-radiative transition probabilities and yields is outdated, the International Atomic Energy Agency (IAEA) called for a coordinate research project with the aim of determining those values more accurately [17]. As a consequence of this, the first aim of this thesis is the determination of updated atomic transition probabilities and energies using the Dirac-Fock method implemented as MCDFGME code [18].

Once the transition probabilities are calculated, we need to obtain the Auger electron spectra resulting from the atomic relaxation cascade. The second objective will then be to use the new transition probabilities in a Monte Carlo program that generates the Auger electron spectra and X-ray emission. As a third objective, we will use the ^{125}I Auger spectra in a simulation of the energy deposited in a simple cell model using the Monte Carlo particle transport code PENELOPE [19]. The results using the new transition probabilities and the EADL database will be compared and discussed.

1.1 Auger-Electron Radionuclide Therapy

To induce cell death in a tumor, critical target molecules like deoxyribonucleic acid (DNA) must be harmed. The mechanism of radiation action in a tumor then depends on the probability of damage induction through direct ionizations of DNA or in its close vicinity, inducing ionization in water molecules and generating reactive oxigen species (e.g. O_2^-, H_2O_2, OH and OH^-) that will ionize target molecules through indirect ionization. A number of different lesions may occur to DNA - single-strand breaks (SSB), double-strand breaks (DSB), base damage, DNA-protein

---

[1] Shake-off and shake-up processes correspond to changes in the effective nuclear charge viewed by the remaining electrons after an electron removal, respectively leading to excitation of atomic electrons into the continuum or into a lesser-bound discrete excited state [11]. These processes are not part of the scope of this thesis so shake-off and shake-up will be only briefly referred.

cross-links and multiply damaged sites (MDS) but only DSB and MDS are not repaired with high fidelity [20]. The harm depends on the nature and energy of the incident particle, and is usually parametrized in terms of the *linear energy transfer* (LET), which represents the energy deposition per unit track length (keV/μm) (Figure 1.2). Alpha particles produce a high number of ionization along a linear path (LET of $\sim$ 80-100 keV/μm), beta-decay electrons usually have low LET ($<$ 1 keV/μm), whereas Auger electrons produce clusters of high ionization density [20] (LET of $\sim$4-26 keV/μm).

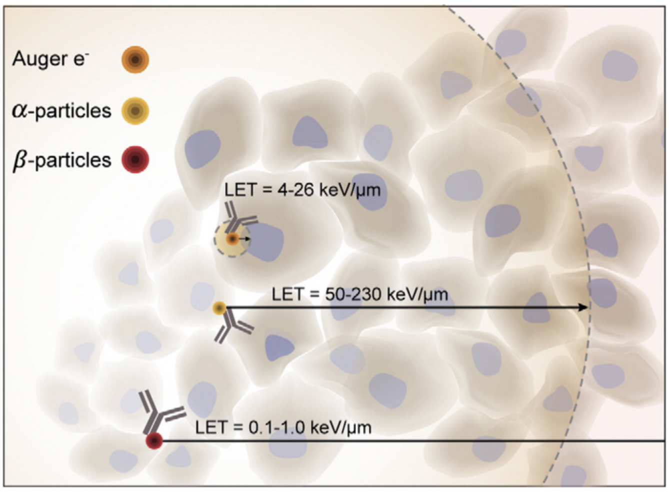

Figure 1.2: Illustration of the track of α, β particles and Auger electrons emitted by radiolabeled monoclonal antibodies targeted to cancer cells [21].

When comparing LET distribution along the path of low-energy β particles and Auger electrons the difference becomes relevant in the nanometer range (Figure 1.3).

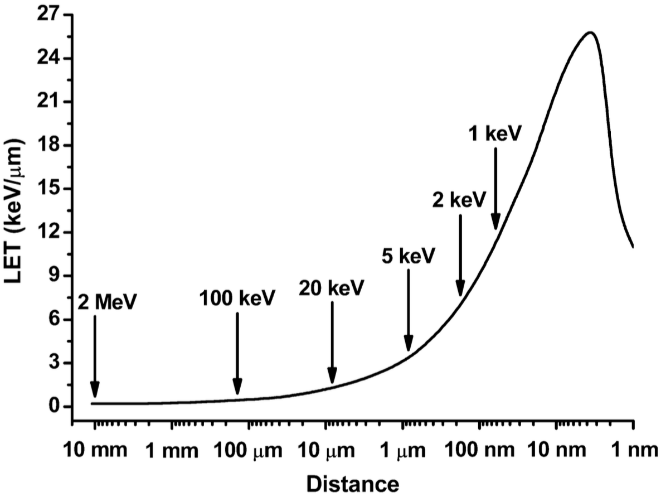

Figure 1.3: Linear energy transfer (LET) along paths of energetic beta particles and Auger electrons as function of traversed distance. For short-range values ($\leq$ 150 nm) LET of Auger electrons is much higher than LET of β particles (with track lengths of $\lessapprox$ 10 mm and LET values of 0.1–1.0 keV/μm) [22].

With regard to the surviving fractions of irradiated cells, Figure 1.4 shows us that, for mammalian cells, the surviving fraction significantly decreases for α particles and DNA-incorporated Auger electrons in a range of 100 Gy, while for X-rays and energetic β particles, similar values of surviving fractions can be achieved but with higher energies up to 500 Gy.

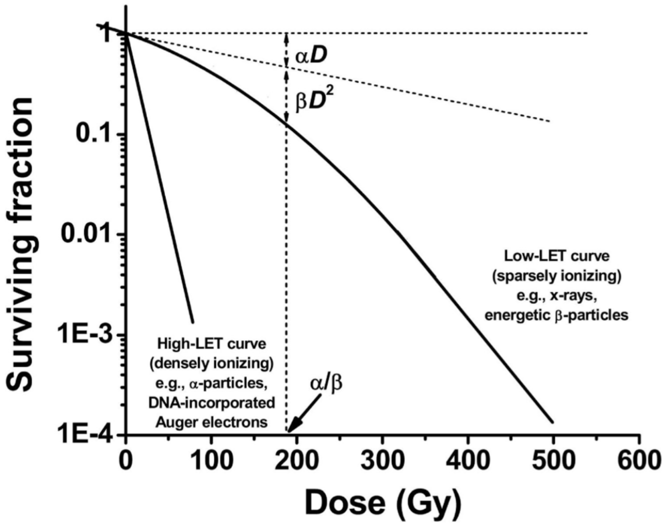

Figure 1.4: Mammalian cell survival curves after low and high LET irradiation. After irradiation with high-LET irradiation with α particles and DNA-incorporated Auger electrons, mammalian cells show exponential decrease in survival [20].

1.1.1 Iodine-125

One of the most studied and used radionuclides in medicine is Iodine-125 (^{125}I) . Due to its low energy photons emitted, ^{125}I is commonly used for low dose rate brachytherapy treatments [23], but since along with the low energy photons, Auger electrons are also emitted, this makes Iodine-125 suitable to targeted radionuclide therapy [24] as well. It has a physical half-life of 54.9 days and decays by 100% EC via the excited level of 35.5 keV of Tellurium-125 (^{125}Te). This excited level has a half-life of 1.6×10^{-9}s, and decays 7% by gamma emission are emitted and 93% by IC electrons into the ground-state of ^{125}Te (see Figure 1.5).

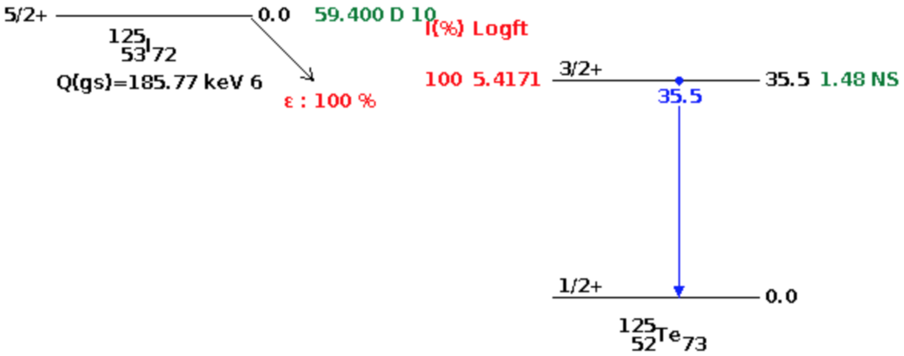

Figure 1.5: ^{125}I decay scheme. Adapted from the National Nuclear Data Center (NNDC) [25].

1.2 Objectives

By the early 60s and thereafter, an increased interest in the therapeutic potential of Auger electron emitters has developed multidisciplinary studies and more complex approaches of biological, chemical and physical nature. Given the very low energy of the emitted Auger electrons, with ranges at micro- and nano-scale, and the difficulty in measuring their yields, theoretical calculations of these values are required. Since the current databases of Auger yields for medical applications is based on outdated atomic and nuclear data, the International Atomic Energy Agency (IAEA) called for a Coordinated Research Project with the aim of determining the energies and emission probabilities of the low-energy X-rays and Auger electrons more accurately. In this way, this work has the following objectives:

- Determination of atomic transition probabilities and energies (Auger and X-ray) using Dirac-Fock method with the state of the art code MCDFGME;
- Simulation of vacancy creation and Auger cascades from a Monte Carlo calculation;
- Comparison of obtained spectra with Evaluated Atomic Data Library (EADL);
- Simulation, at cellular and DNA scale, of dose deposition in a virtual phantom using PENELOPE Monte Carlo code.

1.3 Thesis Outline

In Chapter 2, the calculation methods of atomic fundamental properties are presented, namely the Dirac-Fock method and the relativistic hamiltonian of the atomic system with N electrons studied. The radiative and Auger transition energies, as well as their probabilities are also described in this chapter.

In Chapter 3, the mechanisms that originate vacancies in an internal electron shell and subsequent atomic relaxation process are described. The fundamental atomic parameters related with those processes are presented as well. In the last part of this chapter the concepts of the Monte Carlo algorithm used to generate the atomic cascades are briefly discussed.

In Chapter 4, the results of atomic transition rates and yields for ^{40}Ar and ^{125}I are presented and compared with the ones from EADL database. The obtained Auger and X-ray spectra are also presented.

In Chapter 5 the virtual simple and modified MIRD model used to calculate the Auger electrons dose deposition in a cell through a Monte Carlo simulation with PENELOPE are described. The results are then presented and compared with some of the available literature.

In Chapter 6 the main conclusions of this work are presented and the future work is discussed, with focus on the calculation of atomic parameters and microdosimetric calculations in promising new Auger-emitting radionuclides.

Chapter 2

Calculation of Atomic transitions

In this chapter, the calculation methods to determine atomic fundamental properties are described, namely the Dirac-Fock method. The relativistic hamiltonian of the system is presented together with the description of the radiative and vacuum polarization corrections included in the calculations. The radiative and Auger transition energies and probabilities per unit time used in our calculations are defined in the final part of the chapter.

2.1 Relativistic Calculation of Atomic Properties

To determine the theoretical transition probabilities and energies of X-rays and Auger electrons emitted in a transition, the relativistic atomic theory is currently applied and reproduces well the experimental data. The non-relativistic Hartree-Fock method uses the Schrödinger equation and is not sufficiently accurate in the prediction of atomic properties of light neutral atoms or ions with heavy nuclei. For these atoms and ions, relativistic effects and electron correlation must be taken into account. In the case of heavy atoms, transition energies involving deep inner-shell electrons are not correctly determined if no QED corrections are included.

For atoms with atomic number $Z_{eff} \lesssim 20$ the electron correlation effects dominate and relativistic corrections should be taken into account. Unless extremely high precision is required, QED corrections are negligible. For atoms with $20 \lesssim Z_{eff} \lesssim 60$, relativistic effects alter sufficiently the inner-shell radial functions and, hence, should be included in the calculations. In the case of heavy atoms with $Z_{eff} \gtrsim 60$, electron correlation may be necessary and relativistic effects are dominant.

Relativistic effects and electronic correlation may be significant in the calculation of outer subshell transition probabilities, where the very low energy (high LET) Auger electrons originate. The MCDF method is the relativistic equivalent of Multiconfiguration Hartree-Fock method [26] and is briefly explained in the following section. The MCDFGME code implements the Multiconfiguration Dirac-Fock method, however in this study the full MCDF method will not be used since it is very time consuming. Instead, a description of the atomic wavefunctions that includes mixing electronic configurations with the same J obtained from different jj-couplings will be used. This is a significant improvement over previous calculations like the EADL database that is based on the Dirac-Hartree-Slater (DHS) method.

2.1.1 Dirac-Fock Method

Back in 1928, Douglas Rayner Hartree introduced a procedure to calculate approximate wavefunctions and energies for atoms and ions called *self-consistent* method [27], and, in the same year, John Clark Slater combines the procedure of Hartree with the *variational* principle. In 1939, Slater and Vladimir Aleksandrovich Fock showed Hartree's method did not respect Pauli's principle on the wavefunction symmetry. To solve this problem, Slater and Fock introduced the *slater determinants* as a way of obtaining the total antisymmetric wavefunction and this method is the so-called Hartree-Fock method. This is a non-relativistic method and its relativistic equivalent is the Dirac-Fock Method.

As happens generically in other self-consistent methods, to build-up the wavefunctions of an N-electron system the starting points are the central field one-electron orbitals, which in the relativistic case are the Dirac spinors,

$$\Phi_{n\kappa m}(r,\theta,\varphi) = \tfrac{1}{r}\begin{cases} P_{nk}(r)\chi_{\kappa m}(\theta,\varphi) \\ iQ_{n\kappa}\chi_{-\kappa m}(\theta,\varphi) \end{cases} \tag{2.1}$$

which is a simultaneous wavefunction of $\boldsymbol{j}^2$ and $\boldsymbol{j}_z$. P_{nk} and Q_{nk} are, respectively, the large and small components of the radial function. The quantum numbers j, k and l are related by,

$$\kappa = \begin{cases} -l-1, & j = l+1/2 \\ l, & j = l-1/2 \end{cases} \tag{2.2}$$

The spin-angular functions $\chi_{\kappa m}$ are the 2-component Pauli spherical spinors,

$$\chi_{-\kappa m}(\theta,\varphi) = \sum_{\sigma\pm 1/2} \langle lm-\sigma 1/2\sigma | l1/2jm\rangle Y_l^{m-\sigma}(\theta,\varphi)\phi^{\sigma}, \tag{2.3}$$

with the terms under summation being the Clebsch-Gordan coefficients, the spherical harmonic and one of the two Pauli spinors,

$$\phi^{1/2} = \begin{pmatrix} 1 \\ 0 \end{pmatrix} \qquad \phi^{-1/2} = \begin{pmatrix} 0 \\ 1 \end{pmatrix} \tag{2.4}$$

The spinors defined by Eq. (2.1) are used to build the Configuration State Functions (CSF), which are eigenvalues of the parity Π, angular momentum J and its projection M, and are antisymmetric products of one-electron wavefunctions. The CSF represents a linear combination of Slater determinants,

$$\psi(r_1,...,r_N) \quad = \textstyle\sum_{i=1}^{N_\nu} d_i \begin{vmatrix} \Phi_1^i(r_1) & \cdots & \Phi_N^i(r_1) \\ \vdots & \ddots & \vdots \\ \Phi_1^i(r_N) & \cdots & \Phi_N^i(r_N) \end{vmatrix} \tag{2.5}$$

where ν stands for the number of configurations considered and the coefficients d_i are determined under the requirement that CSF is an eigenstate of $\boldsymbol{J}^2$ and $\boldsymbol{J}_z$. The total MCDF wavefunction is then a superposition of these CSFs. In this work, only the fundamental electronic configurations were considered, so the total MCDF wavefunction are defined by Eq. (2.5), i.e., no excited configurations were considered.

The MCDF solutions are obtained from the variational method applied to the total energy,

$$\Psi(\Pi JM) = \sum_{i=1} d_i \psi(r_1,...,r_N). \tag{2.6}$$

The MCDF wavefunctions are obtained from the total energy, which is calculated through a variational method and it is an eigenvalue of the equation,

$$E = \frac{\langle\Psi|H_{DCB}|\Psi\rangle}{\langle\Psi|\Psi\rangle}, \tag{2.7}$$

where H_{DCB} represents the Dirac-Coulomb Breit Hamiltonian Eq. 2.11 that we will define in the next section. The minimization of that energy is a function of the d_i values in expression 2.5. It is expressed by

$$\delta = \frac{\langle\Psi|H_{DCB}|\Psi\rangle}{\delta d_i \langle\Psi|\Psi\rangle} \tag{2.8}$$

The radial Dirac-Fock equations will be obtained through the minimization of the hamiltonian in order to the radial equations P_{nk} and Q_{nk},

$$\delta = \frac{\left(\delta(\langle\Psi|H_{DCB}|\Psi\rangle - \sum_{ij}\varepsilon_{ij}\langle\psi_i|\psi_j\rangle\right)}{\delta P_{nk}(r)} = 0 \tag{2.9}$$

and

$$\delta = \frac{\left(\delta(\langle\Psi|H_{DCB}|\Psi\rangle - \sum_{ij}\varepsilon_{ij}\langle\psi_i|\psi_j\rangle\right)}{\delta Q_{nk}(r)} = 0, \tag{2.10}$$

where ε_{ij} represents the Lagrange parameters to guarantee the orthogonality of the wavefunctions. With these two equations, a system of differential equations will be obtained for each orbital, leading to the so-called Dirac-Fock equations:

$$\frac{d}{dr}\begin{bmatrix} P_i(r) \\ Q_i(r) \end{bmatrix} = \begin{bmatrix} -\frac{k}{r} & 2c + \frac{\varepsilon_{ij} - V_i(r)}{c} \\ -\frac{\varepsilon_{ij} - V_i(r)}{c} & \frac{k}{r} \end{bmatrix} \begin{bmatrix} P_i(r) \\ Q_i(r) \end{bmatrix} + \begin{bmatrix} X_i^Q(r) \\ X_i^P(r) \end{bmatrix}$$

where $V(r)$ represents the sum of nuclear potencial and Coulomb repulsion, $X^Q(r)$ and $X^P(r)$ represent the general exchange potentials.

The Dirac-Fock equations will then be solved through an iterative self-consistent method. In practice, a set of trial radial functions are used to achieve the initial values of the mixing coefficients d_i while the radial functions are kept frozen, then the coefficients are frozen and the radial functions varied. The process continues until both the radial functions and mixing coefficients have converged to the desired accuracy [28]. The mixing of different configurations in the expansions of the CSF and the total MCDF wavefunctions (see Eqs. (2.5) and (2.6)) partially accounts for the electronic correlation in the MCDF method, which is not present in the EADL calculations based on the DHS approach.

2.1.2 Relativistic Hamiltonian of the System

For a system of N electrons, the relativistic Hamiltonian corresponds to que Dirac-Coulomb Breit hamiltonian given by

$$H_{DCB} = \sum_{a=1}^{N} h_a^D + \sum_{a=1}^{N-1} \sum_{b=a+1}^{N} h_{ab}^{CB}, \tag{2.11}$$

where the Dirac operator H_a^D for the a-th electron is given by

$$h_a^D = c\boldsymbol{\alpha}_a \cdot \boldsymbol{p}_a + \beta_a c^2 + V_a^N, \tag{2.12}$$

with V_a^N the nucleus-electron potential, c the velocity of light and $\boldsymbol{\alpha}_a$ and β_a the four-component Dirac matrices,

$$\boldsymbol{\alpha} = \begin{pmatrix} 0 & \boldsymbol{\sigma} \\ \boldsymbol{\sigma} & 0 \end{pmatrix} \qquad \beta = \begin{pmatrix} I & 0 \\ 0 & -I \end{pmatrix},$$

where I and 0 are, respectively, the 2×2 identity and zero matrices, and $\boldsymbol{\sigma}$ are the Pauli matrices.

The term h_{ab}^{CB}, which is the Coulomb-Breit operator, corresponds to the electron-electron interaction and includes the instantaneous Coulomb repulsion, the magnetic interaction (Gaunt term) and the retardation in the electron-electron interaction due to the finite value of the light speed c respectively. In the Coulomb gauge it has the following expression:

$$h_{ab}^{CB} = \frac{1}{r_{ab}} - \frac{\boldsymbol{\alpha}_a \cdot \boldsymbol{\alpha}_b}{r_{ab}} + \frac{\boldsymbol{\alpha}_a \cdot \boldsymbol{\alpha}_b}{r_{ab}}[\cos(\omega_{ab} r_{ab})] + (\boldsymbol{\alpha} \cdot \boldsymbol{\nabla})_a (\boldsymbol{\alpha} \cdot \boldsymbol{\nabla})_b \frac{\cos(\omega_{ab} r_{ab}) - 1}{\omega_{ab}^2 r_{ab}}, \tag{2.13}$$

where c was taken in atomic units (a.u.) as $c = 1/\alpha$ (with $\alpha \simeq 1/137$ the fine structure constant), ω_{ab} is the frequency of the photon energy exchanged [1].

The MCDFGME code includes the Gaunt and first-order retardation interaction in the self-consistent variational method, and the remaining Breit retardation terms are calculated perturbatively.

---

[1] In an independent model description the frequency of the exchange photon can be given by $\alpha|\varepsilon_i - \varepsilon_j|$

Radiative Corrections

Although the radiative corrections in the calculation of many-electron still represent a more difficult numerical problem to deal with, at least an estimation of these corrections has to be considered for relativistic calculations. The radiative corrections included in the MCDF calculations include two contributions:

- The vacuum polarization, represented by effective potentials from Quantum Electrodynamics (QED);
- The self-energy, for which the first-order contribution is known for hydrogen-like systems.

Vacuum Polarization The vacuum polarization represents an effect of QED. It consists in the creation of virtual electron positron pairs by the mediator of the electromagnetic field, and the absorption of a virtual photon by the electrons in consequence of the annihilation of those particle-antiparticle pairs, illustrated in Figure 2.1. The absorption of the virtual photon will then lead to an energy shift from the theoretical levels predicted by the Dirac theory. This correction was taken into account when using the MCDFGME code.

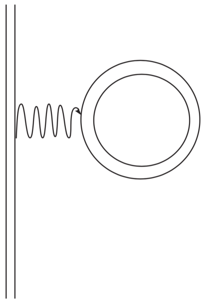

Figure 2.1: Feynman diagram for the first-order Lamb shift of a bound electronic state: vacuum polarization. A virtual electron positron pair is created in the nucleus field and the resulting virtual photon absorbed by the electrons [29].

Self-energy The self-energy effect originates from the interaction of the electron with its own radiation field. The bound electron emits and absorbs a photon immediately afterwards. This effect represents the most significant contribution from QED to the so called *Lamb shift* and has been determined by Peter J. Mohr [30]. This correction was also taken into account when using the MCDFGME code.

2.2 Calculation of atomic transitions

2.2.1 Radiative Transitions

The energy of the photon emitted in a radiative transition between an initial and final one vacancy states i and f is given by

$$E_{if} = E_i - E_f, \tag{2.14}$$

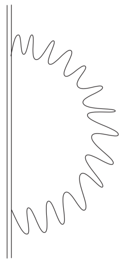

Figure 2.2: Feynman diagram for the first-order Lamb shift of a bound electronic state: self-energy. The bound electron emits and absorbs a photon immediately afterwards [29].

where E_i and E_f correspond to the energies of the initial and final states, respectively.

The transition probabilities per unit time of these radiative transitions can be calculated using a multipole expansion of the matrix element between those initial and final states and the energy of the photon emitted:

$$\begin{aligned} W_{if}^{R} &= \frac{1}{2\pi c} E_{if} \sum_{\lambda=\pm1} \int d\Omega_{\boldsymbol{k}} |\langle \Phi^{\nu_f}_{\Pi_f J_f M_f} | T_\lambda(\boldsymbol{k}) | \Phi^{\nu_i}_{\Pi_i J_i M_i} |^2 \\ &= \frac{4}{3} \left(\frac{E_{if}}{c} \right)^3 \langle \Phi^{\nu_f}_{\Pi_f J_f M_f} | \sum_{a=1}^{N} \boldsymbol{r}_a | \Phi^{\nu_i}_{\Pi_i J_f M_i} \rangle |^2 + \cdots , \end{aligned} \tag{2.15}$$

where $T_\lambda(\boldsymbol{k}) = \sum_{a=1}^{N_e} \boldsymbol{\alpha}_a \cdot \boldsymbol{\epsilon}_\lambda e^{i\boldsymbol{k}\cdot\boldsymbol{r}_a}$ is the operator that describes the emission of a photon with propagation vector $\boldsymbol{k}$ at the electron position $\boldsymbol{r}_a$, and unit polarization $\boldsymbol{\epsilon}_\lambda$. The first term of the expansion is the dominant electric dipole transition. The contribution of the expansion terms of Eq. (2.15) decreases with the rank of expansion terms.

2.2.2 Auger Transitions

From the standpoint of the Lorentz-covariant theory of Quantum Electrodynamics, the Auger effect is produced by the retarded electromagnetic interaction between two bound-state Dirac electrons[2] [31]. In 1931, in his work on relativistic scattering of electrons, Christian Møller treated the radiationless transitions as a time-independent two electron problem: one of the electrons acts as the source of virtual photons with which the second will interact. The interaction operator of the interaction comes:

$$W_{if}^{NR} = 2\pi \frac{\tau}{2j_i + 1} \sum_{\kappa_c} |\mathcal{D}_{if} - \mathcal{E}_{if}|^2, \tag{2.16}$$

where $\mathcal{D}_{if}$ and $\mathcal{E}_{if}$ stand, respectively, for the direct and exchange matrix elements,

---

[2] The electromagnetic interaction consists of a charge-charge interaction (the time-like part of the four-current interaction), or Coulomb interaction, and a current-current or magnetic interaction (the space-like part of the four-current). In the non-relativistic limit, there is only a pure Coulomb interaction. The Auger effect can then be treated as a second order process in QED, for which the matrix element is represented by a second order Feynman diagram with two vertex points.

$$\begin{aligned}\mathcal{D}_{if} &= \langle \phi^a_{n_f \kappa_f j_f} \psi^b_{n_c \kappa_c j_c}; f | V^{CB}_{ab} | \phi^a_{n_i \kappa_i j_i} \phi^b_{n'_i \kappa'_i j'_i}; i \rangle \\ \mathcal{E}_{if} &= \langle \phi^a_{n_f \kappa_f j_f} \psi^b_{n_c \kappa_c j_c}; f | V^{CB}_{ab} | \phi^b_{n_i \kappa_i j_i} \phi^a_{n'_i \kappa'_i j'_i}; i \rangle.\end{aligned} \tag{2.17}$$

The initial state is characterized by two bound electrons with quantum numbers n_i, κ_i, j_i and n'_i, κ'_i, j'_i, and the final state is characterized by a bound electron with quantum numbers n_f, κ_f, j_f and an electron in the continuum with quantum numbers n_c, κ_c, j_c. To avoid double counting, $\tau = 1/2$ if $n_i \kappa_i = n'_i \kappa'_i$ and $\tau = 1$ otherwise. The two-electron operator V_{ab} is chosen to be the Møller operator that is an approximation of the Coulomb-Breit operator including a scattering term,

$$\boldsymbol{V}_{ab} = (1 - \boldsymbol{\alpha}_a \cdot \boldsymbol{\alpha}_b) \frac{e^{ikr_{12}}}{4\pi r_{ab}} \tag{2.18}$$

The continuum electron wave-function in the final state, ψ_{nkm}, is evaluated by solving the Dirac–Fock equations with the same atomic potential as that of the initial state, and is normalized to represent one ejected electron per unit energy. To ensure orthogonality, no orbital relaxation was allowed between the initial and final bound state wave-functions during the calculation of the non-radiative transition rates. These rates were, however, calculated using the correct transition energies obtained in previous independent calculations of initial and final state wave-functions using complete relaxation.

Chapter 3

Calculation of atomic fundamental parameters

In this chapter, the mechanisms that originate vacancies in an internal electron shell, like EC and IC, and subsequent atomic relaxation process are described and an expression for the number of inner-shell vacancies created is presented. The fundamental atomic parameters related with those processes are presented as well. Finally, the concepts of the Monte Carlo algorithm used to generate the atomic cascades are briefly discussed.

3.1 Inner-shell vacancy production

An inner-ionization process leaves the residual atom in an excited state after the creation of an atomic vacancy. Several processes can create these vacancies: photoionization, impact of charged particles, nuclear decay modes such as EC, IC and other processes. For the purpose of using Auger-electron emitting radionuclides for cancer therapy the essential mechanism of atomic ionization will be EC or IC.

3.1.1 Electron Capture

In the EC, the nucleus $(Z+1, A)$ of an atom decays by absorbing an atomic electron and with the emission of a neutrino,

$$(Z+1, A) + e^{-} \rightarrow (Z, A) + \nu_e \tag{3.1}$$

Such that EC can happen from the atomic shell X (with X=K, L, M, N, ...), the released energy must obey the condition

$$E_{\mu} = Q^{+} - E_i - E_X > 0 \tag{3.2}$$

with $Q^+ = [M(Z+1,A) - M(Z,A)]c^2$ being the disintegration energy, which equals the difference of the atomic masses between parent, $M(Z+1,A)$, and daughter, $M(Z,A)$, nuclear ground states, E_i the final nuclear state energy of daughter nucleus and E_X the binding energy of the electron captured in the X shell in daughter atom.

3.1.2 Internal Conversion

When an excited nuclear state de-excites to a lower state, which may represent the ground nuclear state or not, and electromagnetic (EM) transition occurs, the energy released is carried away by a γ-ray with energy given by

$$E_\gamma = (E_i - E_f) - E_r \tag{3.3}$$

with $E_i - E_f$ the difference of energy between the initial and final nuclear states and E_r the recoil energy of the nucleus in its final state and given by

$$E_r = \frac{E_\gamma^2}{2M_N c^2} \tag{3.4}$$

where $M_N(A,Z)$ is the mass of the recoiling daughter nucleus. The recoil energy may be negligible, except for high γ-ray energies and low atomic numbers.

If, however, the de-excitation energy of the nucleus is transferred to an electron in the X-shell (with $X =$K, L$_1$, L$_2$, L$_3$, ...) an IC can happen and an atomic electron is ejected with an energy given by

$$E_{IC,X} = E_\gamma - E_X \tag{3.5}$$

where E_X represents the binding energy of the electron in the X-shell. Since transitions with IC are only possible if $E_{IC,X} > 0$, IC will depend on the atomic subshell from where the emitted electron originates, the atomic number Z and the nuclear transition energy E_γ. The process competes with gamma emission, and its probability increase with multipolarity[1] of the transition and decreases with increasing transition energy.

3.1.3 Number of inner-shell vacancies created

The total number of vacancies initially created in an inner-shell X following an EC decay is given by

$$N_X = P_X + I_{IC,X} = P_X + I_\gamma \alpha_X \tag{3.6}$$

---

[1] The nuclear transition multipolarity can be of two types: *electric* and *magnetic*, specified by the angular momentum quantum number L of the transition photon. If $L = 0, 1, 2, ...$ transition is a *monopole*, *dipole*, quadrupole, octupole, etc. respectively.

where P_X, $I_{ce,X}$ are the electron capture probability and the internal conversion intensity for subshell X; I_γ is the internal conversion intensity for subshell and $\alpha_X = I_{IC,X}/I_\gamma$ is the internal conversion coefficient for the subshell X. The intensities are defined as the number of emissions per decay of the parent nucleus. Data for the nuclear decay parameters were taken from [32].

3.2 Atomic Relaxation

After the inner-shell ionization the remaining excited atom will begin a relaxation process back to the ground state. The energy release will happen via emission of characteristic X-rays (see Figure 3.1 (a)), in the so-called *radiative transitions*, or will be transferred to an outer-shell electron which, by its turn, is ejected as an *Auger electron*. The latter is known as *non-radiative* or *Auger transition* (see Figure 3.1 (b)).

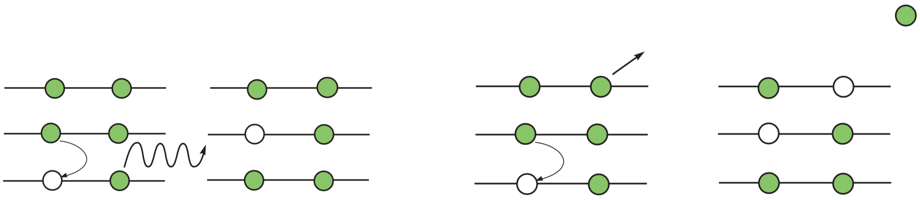
(a) Radiative transition illustration.
(b) Non-radiative transition illustration.

Figure 3.1: Illustration of radiative and non-radiative transitions. The final state of an X-ray transition has one vacancy (a) and the final state of an Auger transition has two vacancies (b) [29].

When the final vacancy of the radiative transition or the two final vacancies of the non-radiative transition are located in the same principal shell of the initial vacancy, the process is called a *Coster-Kronig* (CK) transition.

With regard to the notation used to identify initial and final vacancies, two systems are usually used. In both notations Charles Barkla's designation of shells is followed:

1. Siegbahn: Introduced by Manne Siegbahn in the 1920s, this notation is based upon the relative intensity of spectral lines. In this nomenclature, the initial shell is idenitifed according to Charles Barkla's formalism and the transition by a Greek letter as subscript. The subshell origin of a characteristic X-ray is not identified explicitly (Kα_1, Kα_2, ... ,Kβ_3), which gives it an unsystematic nature;
2. IUPAC: Introduced by the International Union of Pure and Applied Chemistry in 1991 [33], in this notation the shells and subshells are characterised, therefore based upon energy-level designation. A hyphen is used to separate the initial and final states (e.g. K-L$_1$, K-L$_2$, ..., K-M$_1$, ...). The correspondence between shells and IUPAC notation is presented in Table 3.1.

Since EADL transition probabilities were tabulated using IUPAC notation, in what follows this notation will be used. We note that both the Siegbhan and the IUPAC notations assume an one-to-one correspondence between subshell transitions and fine structure electron configurations. However, calculations of atomic transitions between two levels in the MCDF method generally

Subshell	IUPAC	Subshell	IUPAC
$1s_{1/2}$	K	$4p_{3/2}$	N_3
$2s_{1/2}$	L_1	$4d_{3/2}$	N_4
$2p_{1/2}$	L_2	$4d_{5/2}$	N_5
$2p_{3/2}$	L_3	$4f_{5/2}$	N_6
$3s_{1/2}$	M_1	$4f_{7/2}$	N_7
$3p_{1/2}$	M_2	$5s_{1/2}$	O_1
$3p_{3/2}$	M_3	$5p_{1/2}$	O_2
$3d_{3/2}$	M_4	$5p_{3/2}$	O_3
$3d_{5/2}$	M_5	$5d_{3/2}$	O_4
$4s_{1/2}$	N_1	$5d_{5/2}$	O_5
$4p_{1/2}$	N_2	$6s_{1/2}$	P_1

Table 3.1: Subshell correspondence to IUPAC notation. According to the initial and final subshells involved in a radiative or non-radiative transition respectively, IUPAC notation is used generically in the way $X - Y$ and $X - YZ$, where X designates the subshell of the initial vacancy and Y and YZ the subshells of the final vacancies.

involve the mixing of different configurations and, hence, this connection is ambiguous in many cases.

3.2.1 Fundamental atomic parameters

In general several atomic states defined by a J_i value and parity Π_i can belong to a given subshell configuration X. The width, Γ_X, of that subshell is defined as the weighted sum of all individual widths belonging to the subshell,

$$\Gamma_X = \frac{\sum\limits_{i \in X} (2J_i + 1) \sum\limits_{f \in Y} \hbar W_{if}}{\sum\limits_{i \in X} (2J_i + 1)} \tag{3.7}$$

where the sums run over all initial states i belonging to the configuration X ($i \in X$) and all final f states belonging to the configuration Y ($f \in Y$). The fluorescence and Auger yields are defined as the probability that a vacancy in a subshell X is filled through a radiative or radiationless transition, respectively. Being Γ_X^R the radiative transition width of a one-hole state belonging subshell X and Γ_X its correspondent total transition width, the fluorescence yield of that subshell is then defined as

$$\omega_X = \frac{\Gamma_X^R}{\Gamma_X} = \frac{\Gamma_X^R}{\Gamma_X^R + \Gamma_X^{NR}} \tag{3.8}$$

where Γ_X^{NR} represents the non-radiative transition width of the hole in the subshell X.

In a similar way to the fluorescence yield, the Auger yield is defined as the probability that a vacancy in a subshell is filled through a transition of an electron from a higher shell with the concomitant ejection if a second electron from a higher shell too. Thus the Auger yield for a subshell i comes

$$a_X = \frac{\Gamma_X^{NR}}{\Gamma_X^R + \Gamma_X^{NR}} \tag{3.9}$$

From the above definitions of fluorescence and Auger yields, the following relation is satisfied:

$$\omega_X + a_X = 1 \tag{3.10}$$

3.2.2 EADL type formats

In order to our data to be used in the atomic vacancy propagation code, it is required to write it in the EADL type format. The EADL data uses normalized partial widths to describe transition probabilities and average energies to describe one-hole subshell X transitions to higher one-hole subshell Y for radiative transitions and to higher two-hole subshells YZ in the case of Auger transitions,

$$f_{X,YZ}^{NR} = \frac{\Gamma_{X,YZ}^{NR}}{\Gamma_X^R + \Gamma_X^{NR}} \quad \text{and} \quad f_{X,Y}^{R} = \frac{\Gamma_{X,Y}^{R}}{\Gamma_X^R + \Gamma_X^{NR}}, \tag{3.11}$$

where $\Gamma_{XY;Z}^{NR}$ and Γ_{XY}^{R} are the partial widths,

$$\Gamma_{X,YZ}^{NR} = \frac{\sum\limits_{i \in X}(2J_i+1) \sum\limits_{f \in YZ} \hbar W_{if}^{NR}}{\sum\limits_{i \in X}(2J_i+1)} \quad \text{and} \quad \Gamma_{XY}^{R} = \frac{\sum\limits_{i \in X}(2J_i+1) \sum\limits_{f \in Y} \hbar W_{if}^{R}}{\sum\limits_{i \in X}(2J_i+1)} \tag{3.12}$$

Note that by definition,

$$a_X = \sum_{Y,Z} f_{X,YZ}^{NR} \quad \text{and} \quad \omega_X = \sum_{Y} f_{XY}^{R} \tag{3.13}$$

For each subshell transition, we also define the average transition energy:

$$\bar{E}_{XY} = \frac{\sum\limits_{i \in X}(2J_i+1) \sum\limits_{f \in Y} E_{if}}{\sum\limits_{i \in X}(2J_i+1)} \tag{3.14}$$

3.3 Monte Carlo Simulation of Auger-electron Spectra

After an inner-shell ionization, the vacancy created will be most probably filled by an electron from the next highest subshells which, by its turn, will be filled by another electron from a higher subshell. The atomic relaxation is then a process composed of a series of vacancy-filling steps: the de-excitation of an inner-shell hole leads to a cascade of radiative and non-radiative transitions and this cascade can continue until all the vacancies are in the valence-shell or no more atomic transitions are energetically possible. Vacancy cascades usually have lifetimes of 10^{-16} to 10^{-13} seconds [34]. An illustration of the cascade scheme is represented in Figure 3.2.

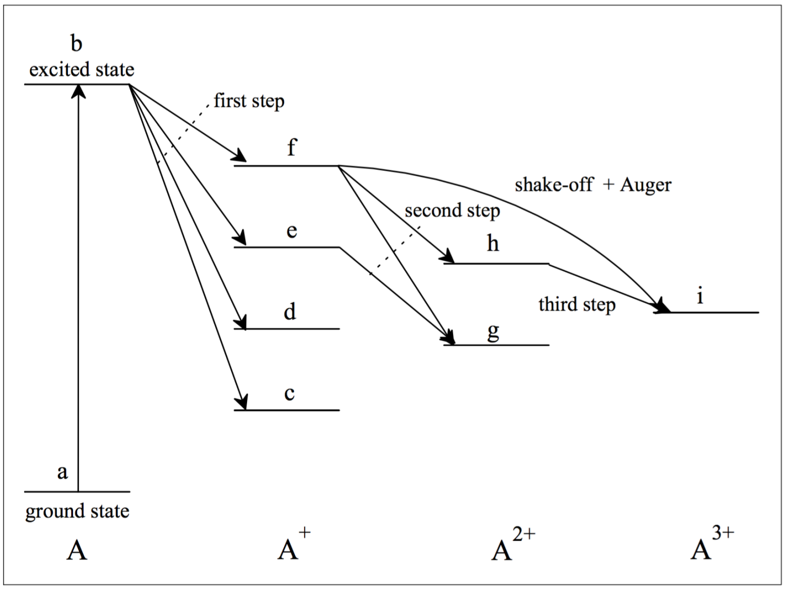

Figure 3.2: Cascade illustration of Auger transitions following excitation of an atom A through $a \rightarrow b$. An A^{+} ion is produced via $b \rightarrow c, d$ transitions, A^{2+} ions via $b \rightarrow e, f \rightarrow g$ and A^{3+} ions via $b \rightarrow f \rightarrow h \rightarrow i$ and $b \rightarrow f \rightarrow i$ processes. The process $f \rightarrow i$ represents a shake-off transition [35].

The first stochastic model of a vacancy cascade was presented in the 1960s by Krause and Carlson [34] and combined aspects of atomic radiations in the neutral atom with the Monte Carlo technique. The calculated charge distributions supported the experimental results and since then the mechanism of vacancy cascade is accepted as stochastic. In spite of that, the majority of existing models of the vacancy cascade are based on the binding energies of neutral-atoms, and then produce discrete distribution of the energy lines instead of a continuous distribution. In fact, the last stage of vacancy cascade in heavy elements will approach a continuum distribution of electron energies [36].

The simulation of the Auger-electron spectrum implies a simulation of the atomic cascade. The simulation of the Auger cascade begins with the atomic configuration of the radionuclide with the shells filled with its Z characteristic electrons. Since the EC process of ^{125}I will create a vacancy in one of the X=K, L, M, N, O shells, the characteristic EC probabilities (conversion coefficients), α_X must be used. The code used to perform the Monte Carlo simulation of cascades takes as input the probabilities for vacancies created in K, L and M, since those are the ones available from the nuclear data sheets [37]. For the simulation, the radiative and Auger transition probabilities and energies obtained with the MCDFGME code, as well as the level widths calculated, are used as input in the EADL format. In this way the simulation develops the following basic steps:

- The sum of the K, L_1 and M_1 conversion coefficients introduced is normalized to 1;

- The occupation values of each shell are established according to the configuration of the desired atomic system;
- The atomic transition rates in the EADL file format are read to generate the X-ray and Auger spectra;
- A number of initial cascade stories (atoms) is defined;
- A random number between 0 and 1 is generated and used to create a vacancy in one of the three shells and according to the EC probabilities introduced for the K, L_1 and M_1 subshells;
- The total transition rate (sum of the radiative and non-radiative rates) calculated for each shell is normalized to 1: each shell vacancy can give rise either to a radiative process or a non-radiative one;
- Another random number between 0 and 1 is generated to select a transition according to the transition probabilities calculated for each subshell;
- A looping in all subshells is processed until the outer subshell is reached or no more electrons are available in the system;
- The frequencies of the X-rays and Auger electrons emitted are recorded in histogram of energy bins;
- The simulation ends when the loop in the independent cascade stories finishes.

The resulting frequency histogram of all energetically possible radiative and Auger transitions accumulated from all cascade stories, produces the output spectra.

3.3.1 Shake-off and Shake-up

Shake-off and shake-up effects result from sudden changes in the central potential of the atom after the removal of an electron by photoionization, EC, IC or radiative and non-radiative transitions. The changes in the effective nuclear charge viewed by the the remaining electrons can lead to the excitation of an atomic electron into a lesser-bound excited state (shake-up) or into its excitation into the continuum (shake-off). In the case, for example, of a photoionization, the interactions between the photoelectron emited and the remaining electrons may decrease the kinetic energy of the photoelectron an the deposition of this energy into the system. The subsequent atomic decays are then called *shake-off* and *shake-up* transitions, and the following phenomena can be related [38]:

- Photoionization and shake-up with Auger decay. In this case, part of the photoelectron energy is absorbed by the atom or added to the energy of the Auger electron;
- Photoionization and shake-off. A free electron is emitted and the atom becomes doubly ionized;
- Photoionization and double Auger transition. In this case, the atom can be triple ionized as a result of the Auger cascade, single Auger transition combined with shake-off or virtual inelastic scattering.

The shake-up and shake-off processes were not taken into account in this work and are only referred in the context of the atomic relaxation.

Chapter 4

Atomic transition probabilities and yields for argon-40 and tellurium-125

In this chapter, the results of the calculated radiative and Auger transition probabilities and rates, yields and subshell widths are presented for two singly-ionized elements in study, ^{40}K-Ar and ^{125}I-Te, with the first having been used to validate and streamline the workflow of the atomic transitions properties calculations and the generation of spectra. The same workflow is then applied to study the more complex ^{125}I, as a suitable radionuclide to be used for targeted Auger electron therapy. The calculated data using MCDFGME code [18] is then benchmarked with the correspondent EADL data available, derived from Chen *et al* calculations [6, 7, 9, 10].

The results of the MC atomic cascades using the code described in Section 3.3 are also showed for either elements, ^{40}Ar and ^{125}Te, to infer on the major differences between their MCDFGME and EADL spectra.

4.1 Atomic Transitions of ^{40}Ar

Due to its low atomic number, closed shells and low number of atomic transitions, ^{40}K was used to validate and optimize the workflow of MCDFGME and MC cascade code usage, as well as the data conversion to EADL data tables format. In total, 21 radiative and 84 radiationless transition probabilities and energies were calculated using MCDFGME code with the hamiltonian corrections described in Section 2.1.2.

^{40}K has a physical half-life of 1.2504$\times$10^9 years and decays by 89.25% β^- to ^{40}Ca, 10.55% EC to the 1460 keV level of ^{40}Ar and 0.2% to the ground state level of ^{40}Ar, and by 0.001% β^+ to the ground state as well. In this case, the study was focused on the EC decay of ^{40}K, a state in which an atomic vacancy is created.

4.1.1 Auger Transition Probabilities

The Auger transition probabilities per decay of ^{40}K were obtained according to equation 3.11 and the results are shown in Figure 4.4. The comparison with the correspondent EADL data is presented in Figures 4.2 and 4.3.

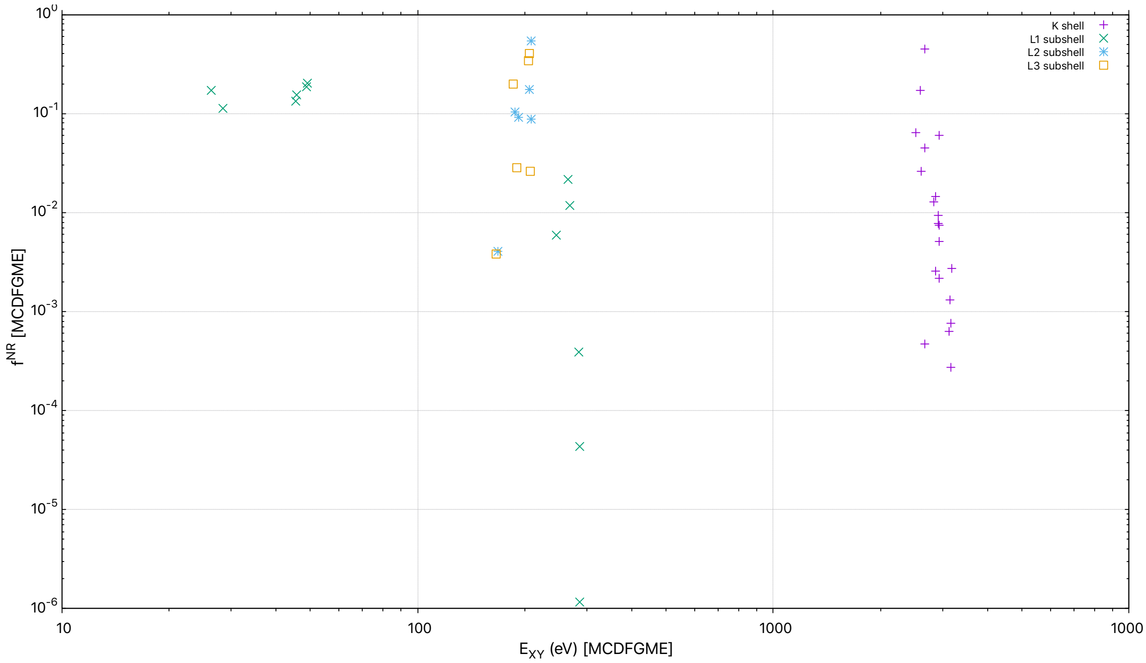

Figure 4.1: Normalized Auger transition probabilities, f^{NR}_{MCDFGME}, for ^{40}Ar as a function of MCDFGME average transition energies $\bar{E}_{XY}$ in eV.

The results of the full relativistic calculation of the Auger transition probabilities show that, for ^{40}Ar and as expected, the transition probabilities for internal subshells are more likely to occur and with higher transition energies. For initial vacancies in the L_3 subshell the range of transition probabilities values is lower.

From the results presented in Figure 4.2, the highest absolute ratios between MCDFGME and EADL transition rates were found for the initial K, L_1 and L_3 vacancies with correspondent ratios of 10.743, 9.591 and 6.802 for L_2-M_3M_3, L_3-M_2M_2 and L_2-M_1M_3 transitions, respectively, but the highest variability in a per subshell basis arises for L_2 subshell.

With regard to the ratios between MCDFGME and EADL transition probabilities of ^{40}Ar Auger transitions, the lowest values were found for the L_1 subshell but te highest variability in a per subshell basis was found for the L_2 subshell.

4.1.2 Radiative Transition Probabilities

The radiative probabilities (per decay of ^{40}K) were obtained according to equation 3.11 and the results are presented in Figure 4.4. The comparison with the correspondent EADL data is shown in Figures 4.2 and 4.3.

The results of the full relativistic calculation of the radiative transition probabilities show that, for ^{40}Ar and as expected, the transition probabilities for internal subshells are more likely to occur

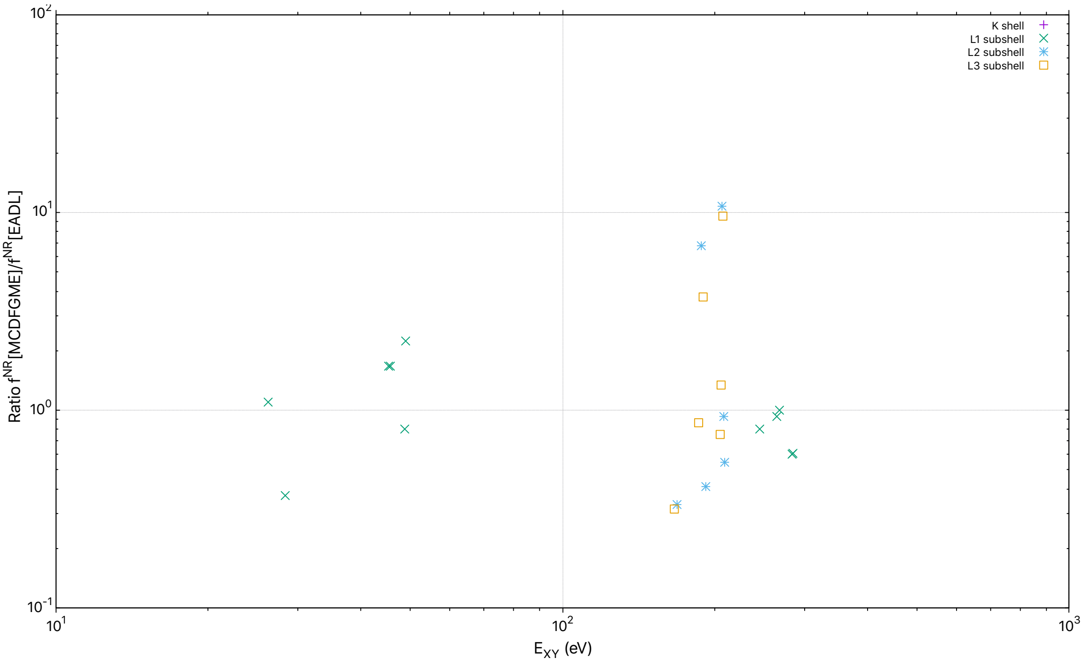

Figure 4.2: Ratio of the normalized Auger transition probabilities, $f^{NR}_{\text{MCDFGME}}/f^{NR}_{\text{EADL}}$, for ^{40}Ar as a function of MCDFGME average transition energies $\bar{E}_{XY}$ in eV.

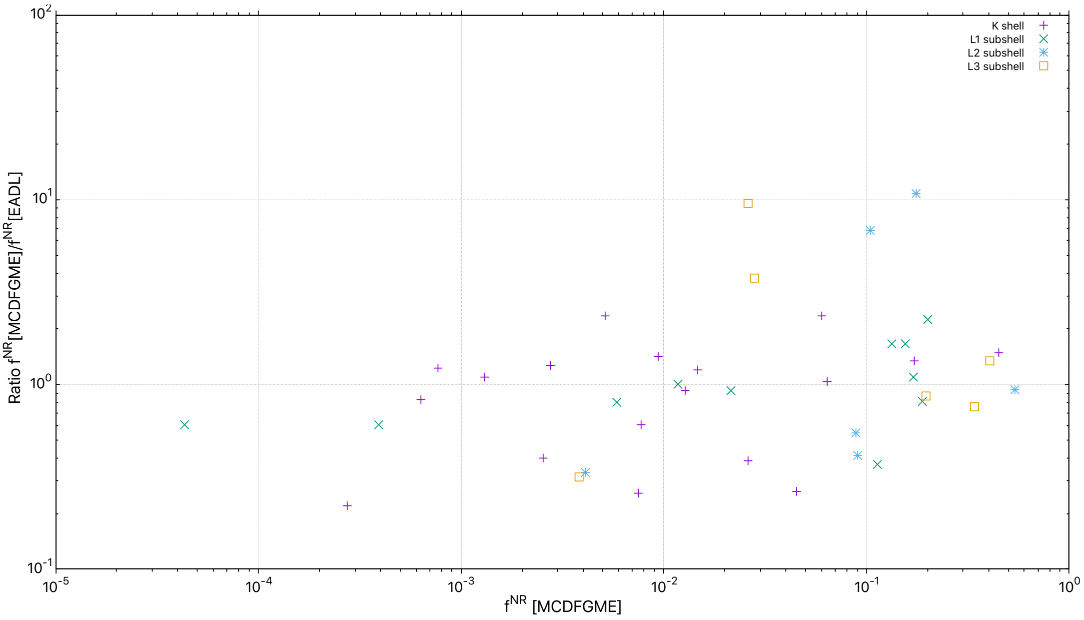

Figure 4.3: Ratio of the normalized Auger transition probabilities, $f^{NR}_{\text{MCDFGME}}/f^{NR}_{\text{EADL}}$, for ^{40}Ar as a function of MCDFGME average normalized transition probabilities f^{NR}_{MCDFGME}.

and with higher transition energies.

From the results presented in Figure 4.5, the highest absolute ratio values between MCDFGME and EADL data was found for the transitions L$_1$-L$_2$ and L$_1$-L$_3$ with correspondent ratios of 0.0371 and 0.0301, respectively. In a per subshell basis, this highest variance is also seen for the L$_1$ subshell.

In the same way than what was determined for the ratio of radiative transition rates as a function of the MCDFGME transition energies, the major differences between the full relativistic results

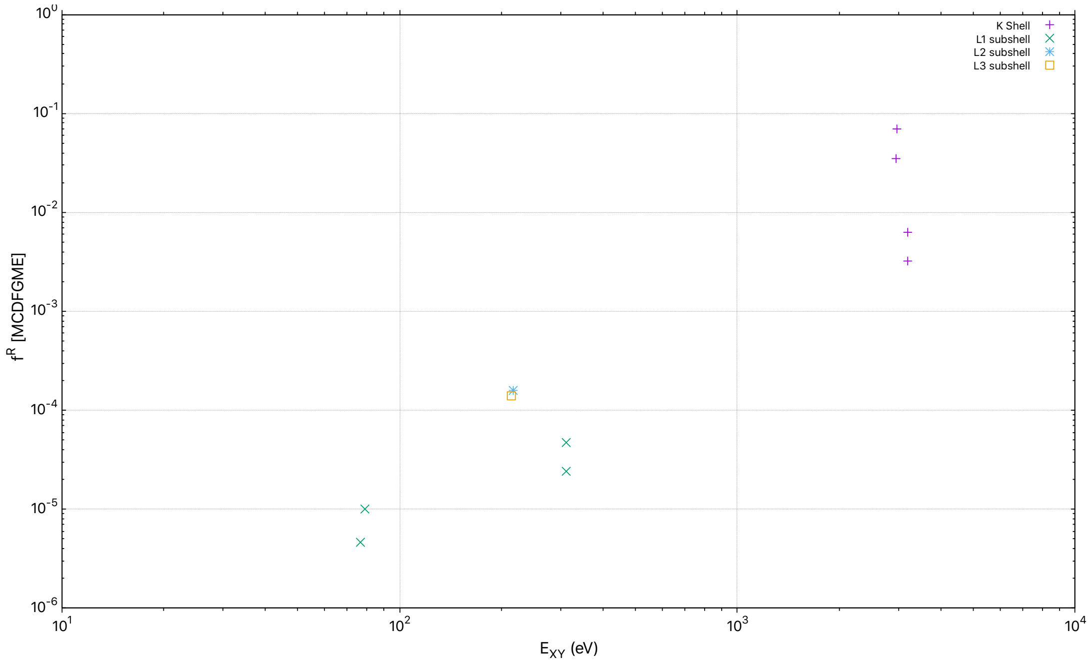

Figure 4.4: Normalized radiative transition probabilities, f^R_{MCDFGME}, for ^{40}Ar as a function of MCDFGME average transition energies $\bar{E}_{XY}$ in eV.

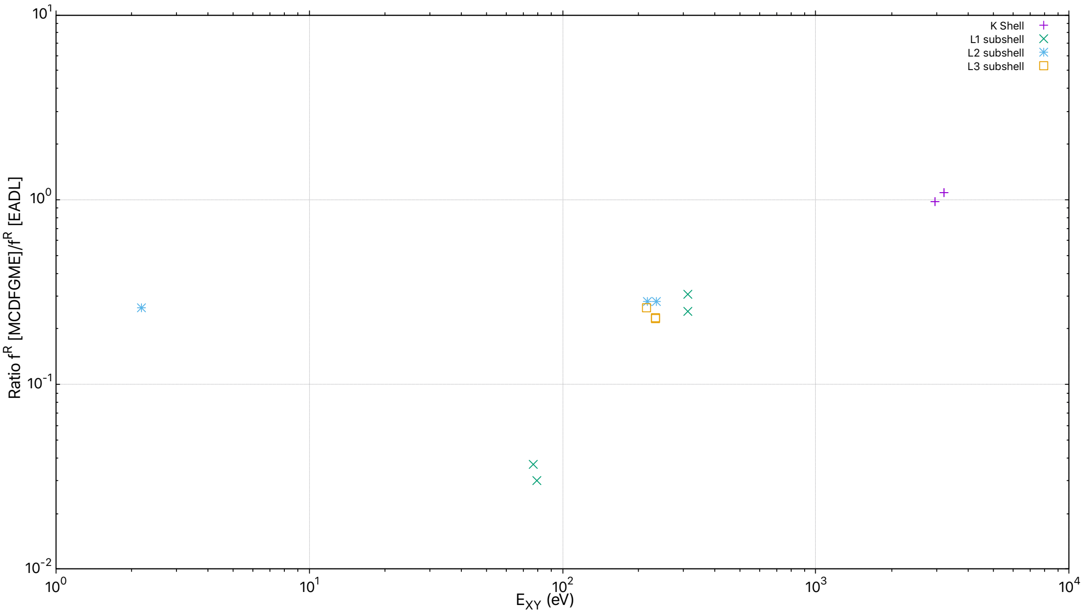

Figure 4.5: Ratio of the normalized radiative transition probabilities, $f^R_{\text{MCDFGME}}/f^R_{\text{EADL}}$, for ^{40}Ar as a function of MCDFGME average transition energies $\bar{E}_{XY}$ in eV.

of MCDFGME and the correspondent values taken from EADL data tables was found for the initial L$_1$ vacancy.

4.1.3 Atomic Shell Widths

The radiative and Auger shell widths of ^{40}Ar were obtained according to the equations 3.12. The results are presented in Table 4.1.

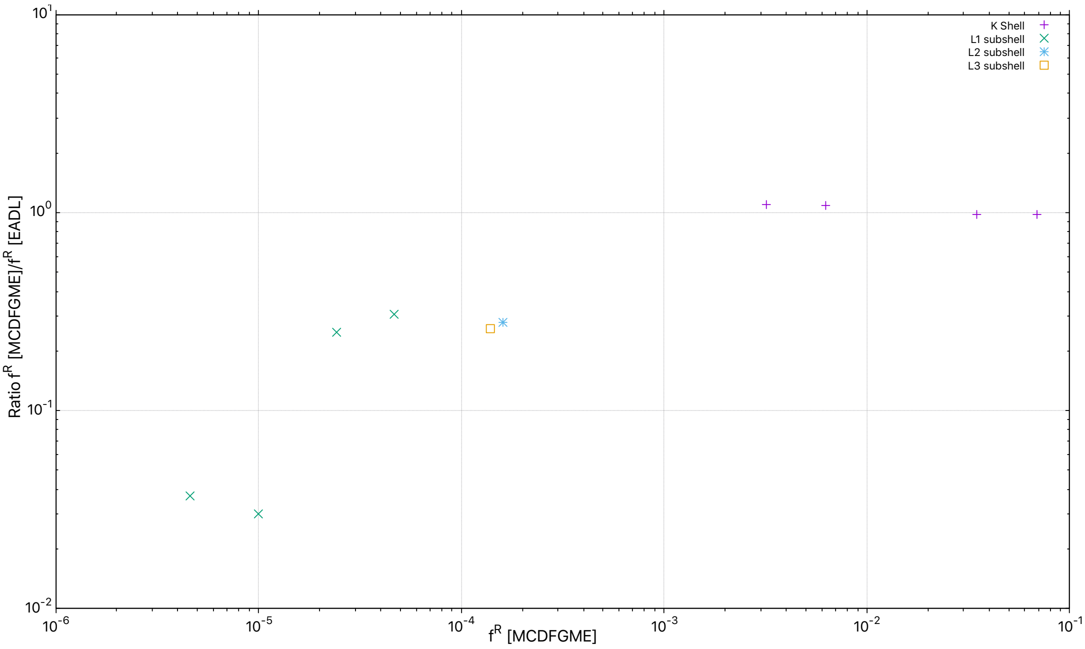

Figure 4.6: Ratio of the radiative transition probabilities, $f^{NR}_{\text{MCDFGME}}/f^{NR}_{\text{EADL}}$, for ^{40}Ar as a function of MCDFGME average transition probability f^{R}_{MCDFGME}.

Table 4.1: Radiative (R) and Auger (NR) sububshell widths for ^{40}Ar in eV.

Subshell	MCDFGME		EADL		Relative Difference	
X	Γ^{R}_{X} [eV]	Γ^{NR}_{X} [eV]	Γ^{R}_{X} [eV]	Γ^{NR}_{X} [eV]	$\Delta\Gamma^{R}_{X}$ [%]	$\Delta\Gamma^{NR}_{X}$ [%]
K	7.651×10^{-2}	5.996×10^{-1}	7.166×10^{-2}	5.576×10^{-1}	6.77	7.53
L_1	2.785×10^{-4}	3.253	2.380×10^{-4}	3.242	17.02	0.34
L_2	2.133×10^{-5}	1.335×10^{-1}	2.435×10^{-5}	1.505×10^{-1}	-12.40	-11.30
L_3	1.804×10^{-5}	1.293×10^{-1}	2.481×10^{-5}	1.513×10^{-1}	-27.29	-14.65
M_1	6.308×10^{-6}	-	-	-	-	-
M_2	3.459×10^{-17}	-	-	-	-	-

According to the results for the shell widths of ^{40}Ar, the calculated values derived from MCDFGME code are in accordance with the ones taken from EADL, with all the values in the same order of magnitude. Nevertheless, and as expected, for the outer shells the relative differences are higher and with values down to -27.29% of difference for radiative transitions and -14.65% for Auger transitions from the initial L_3 subshell.

4.1.4 Auger Yields

The Auger yields of ^{40}Ar subshells were calculated using equation 3.9 and the results can be found in Tables 4.2 and 4.3. The Auger yields of the shells correspond to the average of the subshell yields weighted by its total number of electrons.

The results of the Auger yields for the K and L (sub)shells and the calculated relative differences between the MCDFGME and EADL show that the first are in agreement with the calculated

Table 4.2: Subshell Auger yields for ^{40}Ar.

Yields	a_{K}	a_{L_1}	a_{L_2}	a_{L_3}
This work	8.868×10^{-1}	9.999×10^{-1}	9.998×10^{-1}	9.999×10^{-1}
From EADL	8.854×10^{-1}	9.993×10^{-1}	9.994×10^{-1}	9.995×10^{-1}

Table 4.3: Shell Auger yields for ^{40}Ar.

Yields	a_{K}	a_{L}
This work	8.868×10^{-1}	6.666×10^{-1}
From EADL	8.854×10^{-1}	6.663×10^{-1}
Rel. Diff. [%]	0.16	0.05

EADL values.

4.1.5 Radiative Yields

The radiative yields of ^{40}Ar subshells were calculated using equation 3.9 and the results can be found in Tables 4.4 and 4.5. Like for the Auger yields, the radiative yields of the shells correspond to the average of the subshell yields weighted by its total number of electrons.

Table 4.4: Subshell fluorescence yields for ^{40}Ar.

Yields	ω_{K}	ω_{L_1}	ω_{L_2}	ω_{L_3}
This work	1.132×10^{-1}	8.561×10^{-4}	1.598×10^{-4}	1.396×10^{-4}
From EADL	1.146×10^{-1}	7.070×10^{-4}	5.716×10^{-4}	5.394×10^{-4}
Chen *et al*	1.146×10^{-1}	7.070×10^{-4}	5.716×10^{-4}	5.394×10^{-4}

Table 4.5: ^{40}Ar: Fluorescence yields for K and L shells and the correspondent relative differences between MCDFGME values and some fluorescent yields from the available literature.

Source	Fluorescent yields		Rel. Diff. MCDFGME-Source	
Yields	ω_{K}	ω_{L}	Δ_K[%]	Δ_L[%]
This work	1.132×10^{-1}	3.341×10^{-4}	-	-
From EADL	1.146×10^{-1}	4.190×10^{-4}	-1.22	-20.27
Chen *et al*	1.146×10^{-1}	4.190×10^{-4}	-1.22	-20.27
Bambynek *et al* (1972) [39]	1.150×10^{-1}	-	-1.59	-
McGuire (1970) [40]	1.260×10^{-1}	-	-10.16	-
Kostroun *et al* (1971) [41]	1.110×10^{-1}	-	1.98	-

According to the results shown in Tables 4.4 and 4.5, the radiative yields for the K shell are in accordance with the literature, with relative differences from -10.16 to 1.98%. Nevertheless, for the ω_L value, the discrepancy with the EADL values is higher, with relative differences around -20.27%.

4.2 Atomic Transitions of ^{125}Te

To calculate the radiative and Auger transition probabilities (per decay of ^{125}I), the correspondent yield values and shell widths of ^{125}Te, the energies of 13 172 radiative transitions and 152 481 Auger transitions were calculated using MCDFGME code with the hamiltonian corrections described in Section 2.1.2.

4.2.1 Auger Normalized Transition Probabilities

The Auger normalized transition probabilities per decay of ^{125}I were obtained according to equation 3.11 and the results are presented in Figure 4.7 and in Figures 4.8 and 4.9 in terms of ratios with the correspondent EADL data.

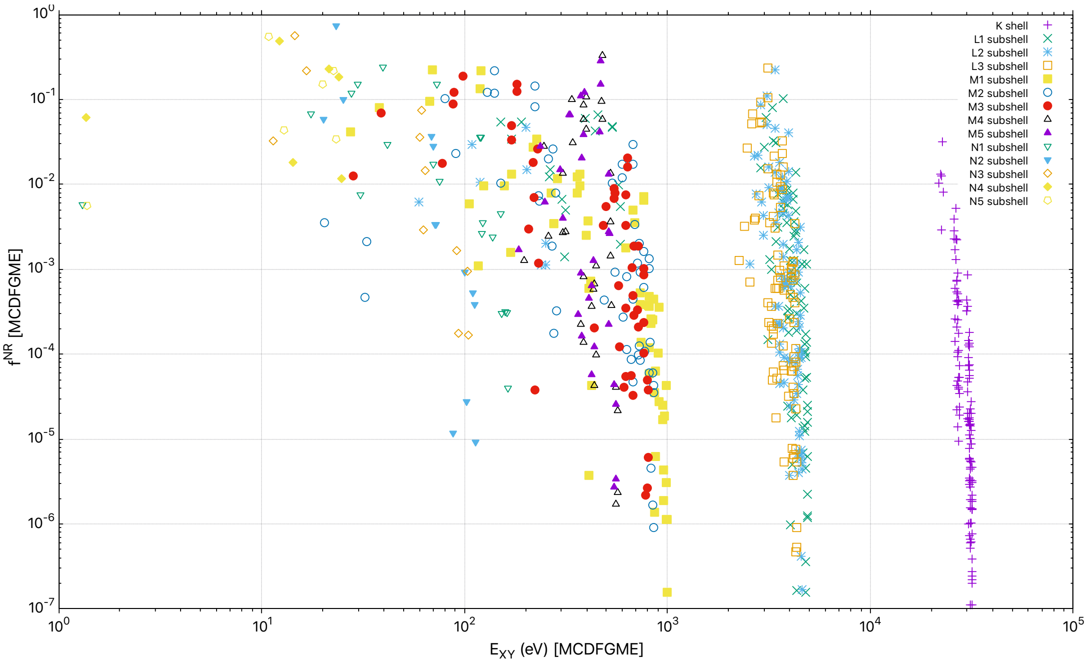

Figure 4.7: ^{125}Te: Auger normalized transition probabilities $f^{NR}_{MCDFGME}$ as a function of MCDFGME transition energies E_{XY} [eV].

The results of the full relativistic calculation of the Auger normalized transition probabilities show that, for ^{125}Te and as expected, the transition probabilities for internal subshells are more likely to occur and with higher transition energies. For initial vacancies in the L$_{1-3}$ subshells the values fall into the same range of probabilities, whilst for M$_{1-5}$ subshells the transition probabilities show rather more variability. With regard to the transition energies and as expected, the transition energies decrease for the outer shells.

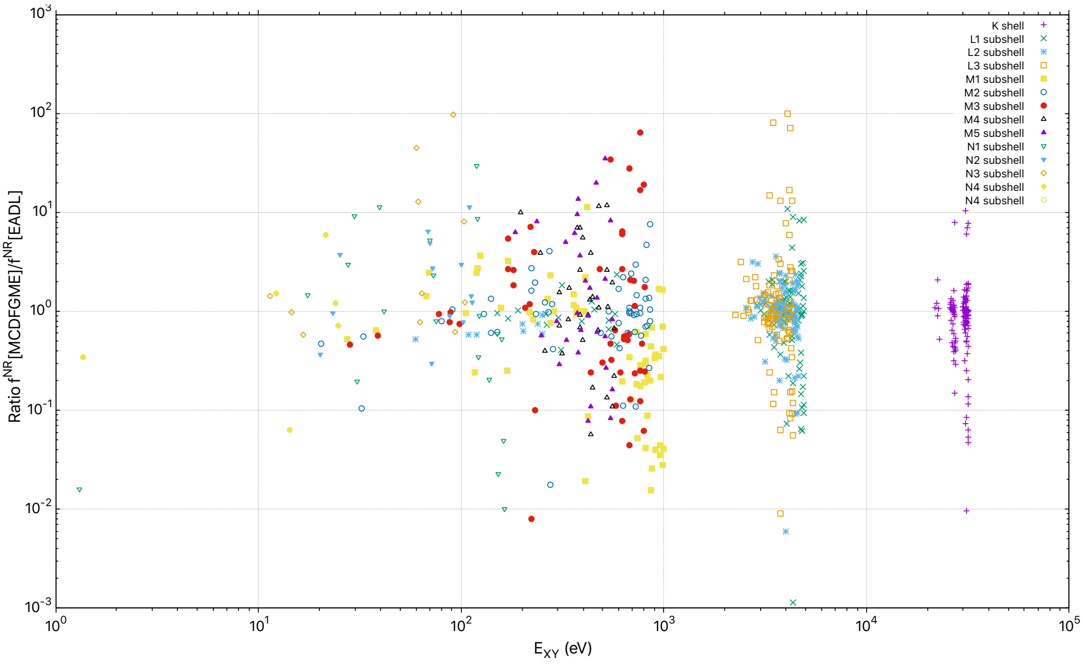

Figure 4.8: ^{125}Te: Comparison of Auger normalized transition probabilities as a function of MCDFGME transition energies E_{XY}. The presented data correspond to the common transitions between MCDFGME transition rates and the correspondent EADL values.

From the calculated ratios between the MCDFGME Auger normalized transition probabilities and the correspondent values taken from EADL data tables presented in Figure 4.8, the trend of variations is in accordance to what was expected, with some ratios close to or higher than 100 for M and N shells. These differences between MCDFGME results and the equivalent EADL data were indeed expected for the outer shells of ^{125}Te.

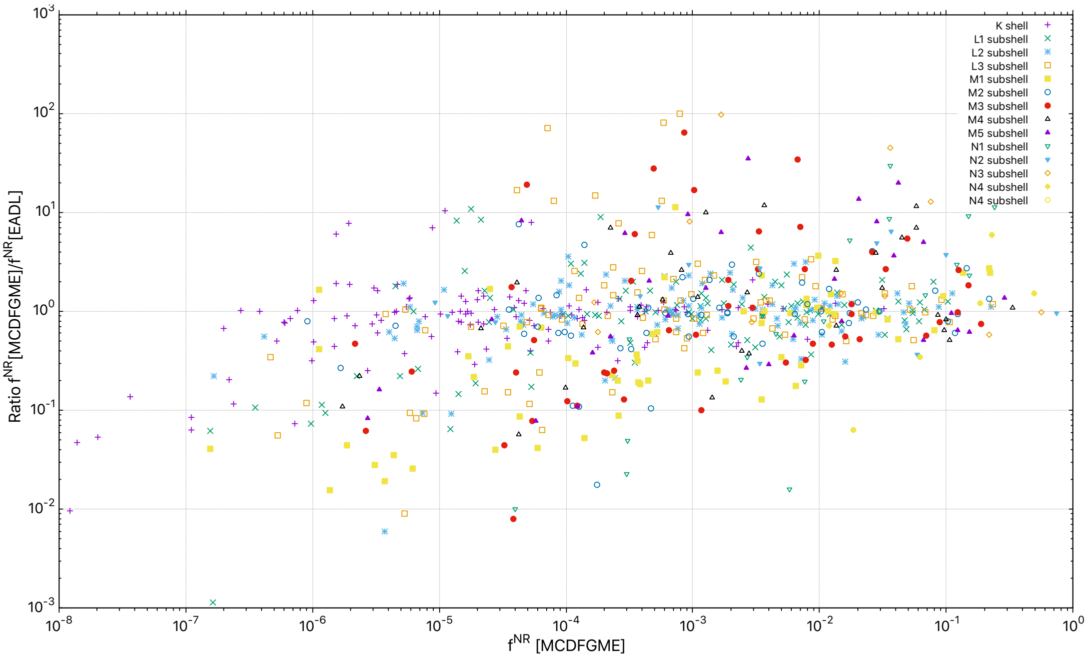

Figure 4.9: ^{125}Te: Comparison of Auger transition rates as a function of MCDFGME transition probabilities f_{ij}^{NR}. The presented data correspond to the common transitions between MCDFGME transition rates and the correspondent EADL values.

From the results presented in Figure 4.9, the discrepancy with the EADL data becomes less evident as a per shell comparison but more explicit for the lower transition probability values, correspondent to the Auger transitions with the outer shells. This trend of variations is then in accordance with what was expected and with the results of Figure 4.8 as well.

4.2.2 Radiative Transition Probabilities

The normalized radiative transition probabilities were obtained according to equation 3.11 and the results are presented in Figure 4.10. In Figures 4.11 and 4.12 the ratios between MCDFGME and the correspondent EADL data are shown as a function of the transition energies and transition probabilities, respectively.

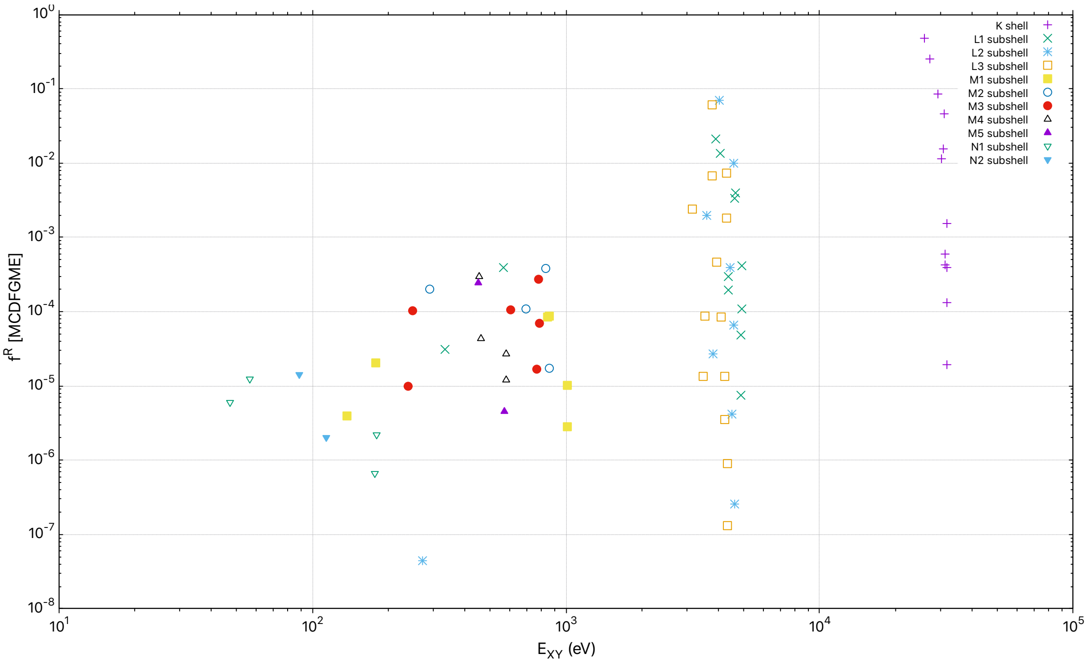

Figure 4.10: ^{125}Te: Radiative normalized transition probabilities $f^R_{MCDFGME}$ as a function of MCDFGME transition energies E_{XY} [eV].

The results of the full relativistic calculation of the radiative normalized transition probabilities show that, for ^{125}Te and as expected, the transition probabilities for internal subshells are more likely to occur and with higher transition energies. In a similar way to the Auger transitions, for initial vacancies in the L_{1-3} subshells the values fall into the same range of probabilities, whilst for M_{1-5} subshells the transition probabilities show rather more variability. With regard to the transition energies and as expected, the transition energies decrease for the outer shells.

The results presented for the calculated ratios between the MCDFGME radiative normalized transition probabilities and the correspondent values taken from EADL data tables, the trend of variations is according to what was expected, with the highest ratios found the for M and N shells. These differences between MCDFGME results and the equivalent EADL data were indeed expected for the outer shells M and N of ^{125}Te, with ratios lower than 0.1 for M_5 subshell and higher than 10 for N_2 subshel.

In terms of the ratios between MCDFGME and EADL transition rates values as a function of

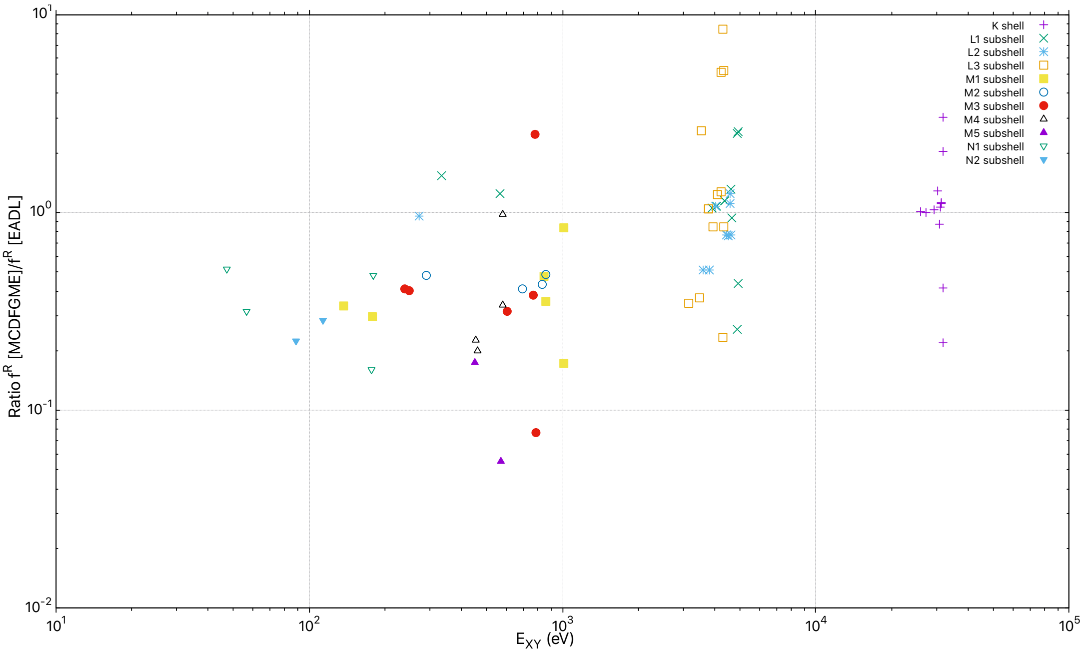

Figure 4.11: ^{125}Te: Comparison of radiative normalized transition probabilities as a function of MCDFGME transition energies E_{XY}. The presented data correspond to the common transitions between MCDFGME transition rates and the correspondent EADL values.

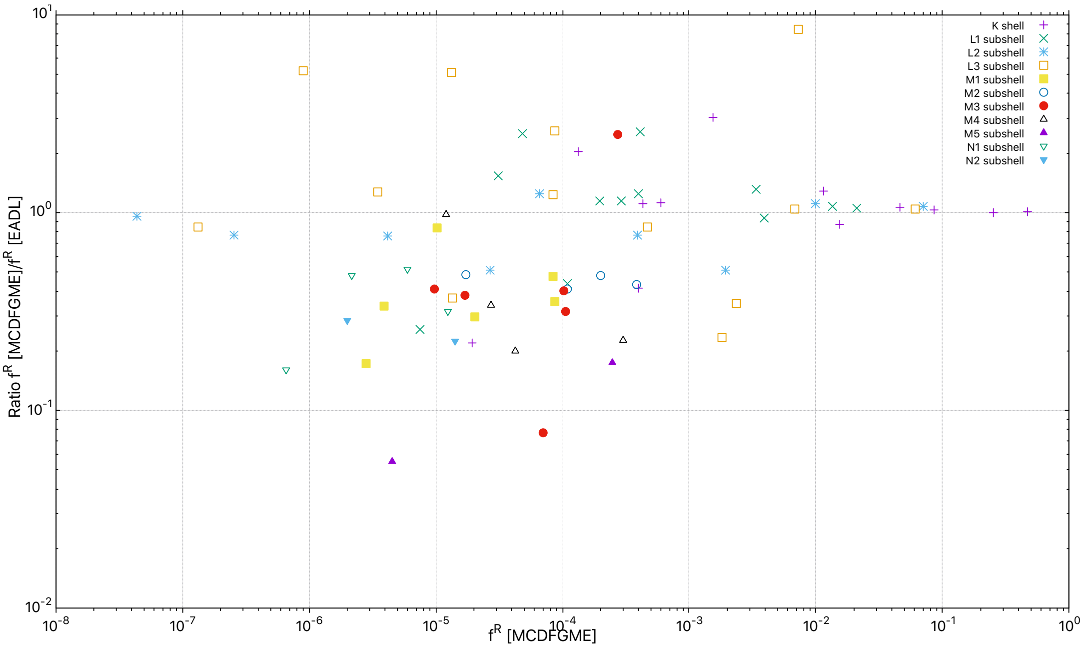

Figure 4.12: ^{125}Te: Comparison of radiative transition rates as a function of MCDFGME transition probabilities f_{ij}^{NR}. The presented data correspond to the common transitions between MCDFGME transition rates and the correspondent EADL values.

the transition probabilities, the results shown in Figure 4.12 are in accordance to what was expected: the lower transition probabilities, correspondent to the radiative transitions with the outer shells, have the highest variations relative to EADL data. Although less evident per shell, the ratios become higher with the lower radiative transition probabilities.

4.2.3 Atomic shell widths

The radiative and Auger widths of ^{125}Te shells were obtained using equations 3.12. The results are shown in Table 4.6 together with the correspondent radiative and Auger shell widths taken from EADL data tables. The Auger yields of the shells correspond to the average of the subshell yields weighted by its total number of electrons.

Table 4.6: ^{125}Te: Shell widths [eV] for K, L_{1-3}, M_{1-5}, N_{1-5} and O_{1-3} subshells.

Subshell	MCDFGME		EADL		Relative Difference	
X	Γ_X^R [eV]	Γ_X^{NR} [eV]	Γ_X^R [eV]	Γ_X^{NR} [eV]	$\Delta\Gamma_X^R$ [%]	$\Delta\Gamma_X^{NR}$ [%]
K	8.503	1.080	8.400	1.236	1.23	-12.62
L_1	1.326×10^{-1}	2.936	1.323×10^{-1}	3.139	0.23	-6.47
L_2	2.304×10^{-1}	2.540	2.224×10^{-1}	2.590	3.60	-1.93
L_3	2.161×10^{-1}	2.508	2.103×10^{-1}	2.377	2.76	5.51
M_1	3.133×10^{-3}	$1.499\times10^{+1}$	2.987×10^{-3}	1.320×10^{-1}	4.89	5.51
M_2	3.330×10^{-3}	4.681	3.011×10^{-3}	4.637	10.59	0.95
M_3	3.249×10^{-3}	5.615	2.951×10^{-3}	5.052	10.10	11.14
M_4	2.034×10^{-4}	5.307×10^{-1}	2.275×10^{-4}	5.146×10^{-1}	-10.59	3.13
M_5	1.722×10^{-4}	5.350×10^{-1}	1.961×10^{-4}	5.183×10^{-1}	-12.19	3.22
N_1	8.542×10^{-5}	4.006	6.418×10^{-5}	$1.344\times10^{+1}$	33.09	-70.19
N_2	2.469×10^{-4}	$1.349\times10^{+1}$	1.810×10^{-4}	$2.520\times10^{+1}$	36.41	-46.47
N_3	2.050×10^{-4}	8.544	1.429×10^{-4}	$3.608\times10^{+1}$	43.46	-76.32
N_4	3.180×10^{-6}	1.317×10^{-1}	2.781×10^{-6}	1.747×10^{-2}	14.35	653.86
N_5	1.596×10^{-11}	1.350×10^{-1}	2.426×10^{-6}	1.951×10^{-2}	-100.00	591.95
O_1	4.167×10^{-6}	-	-	-	-	-
O_2	2.698×10^{-15}	-	-	-	-	-
O_3	2.615×10^{-16}	-	-	-	-	-

The presented results for the ^{125}Te shell widths are in accordance with the correspondent values from EADL data tables, with the exception being the fact that, for EADL data tables, no O shell widths were available.

4.2.4 Auger Yields

The Auger yields were obtained according to equation 3.9 for the K, L M and N shells and the results compared with the ones calculated from EADL data for ^{125}Te in Tables 4.7 and 4.8.

Table 4.7: ^{125}Te: Auger yields for K, L_{1-3}, M_{1-5} and N_{1-5} subshells

Yields	a_{K}	a_{L_1}	a_{L_2}	a_{L_3}	a_{M_1}
This work	1.125×10^{-1}	9.566×10^{-1}	9.168×10^{-1}	9.206×10^{-1}	9.986×10^{-1}
From EADL	1.213×10^{-1}	9.596×10^{-1}	9.209×10^{-1}	9.191×10^{-1}	9.995×10^{-1}
Krause (1979) [42]	1.230×10^{-1}	5.040×10^{-1}	7.710×10^{-1}	9.260×10^{-1}	
Yields	a_{M_2}	a_{M_3}	a_{M_4}	a_{M_5}	a_{N_1}
This work	9.992×10^{-1}	9.993×10^{-1}	9.855×10^{-1}	9.856×10^{-1}	8.855×10^{-1}
From EADL	9.984×10^{-1}	9.983×10^{-1}	9.984×10^{-1}	9.985×10^{-1}	9.999×10^{-1}
Yields	a_{N_2}	a_{N_3}	a_{N_4}	a_{N_5}	
This work	9.675×10^{-1}	9.429×10^{-1}	9.999×10^{-1}	1.000	
From EADL	1.000	1.000	1.000	1.000	

Table 4.8: ^{125}Te: Auger yields for K, L, M and N shells.

Yields	a_{K}	a_{L}	a_{M}	a_{N}
This work	1.125×10^{-1}	6.253×10^{-1}	5.967×10^{-1}	5.673×10^{-1}
From EADL	1.213×10^{-1}	6.264×10^{-1}	5.993×10^{-1}	6.000×10^{-1}
Rel. Diff. [%]	-7.26	-0.18	-0.44	-5.45

The calculated results shown for the MCDFGME Auger yields are in accordance with the correspondent yields taken from EADL data tables. Nevertheless, for the K and L_{1-3} subshells, a comparison with the results from Krause [42] indicate higher relative differences of -9.33% for K shell and 47.31% and 15.90% for L_1 and L_2 subshells, respectively.
In what concerns the Auger shell yields, the highest differences were found for K and N shells and with -7.82% and -5.76% respectively.

4.2.5 Radiative Yields

The Radiative yields were obtained according to equation 3.8 for the the K, L, M and N and O shells and the values compared with the existing data. The results are shown in Table 4.9. Like for the Auger yields, the radiative yields of the shells correspond to the average of the subshell yields weighted by its total number of electrons.

Table 4.9: ^{125}Te: Fluorescence yields for K, L_{1-3}, M_{1-5}, and N_{1-5} subshells.

Yields	ω_{K}	ω_{L_1}	ω_{L_2}	ω_{L_3}	ω_{M_1}
This work	8.874×10^{-1}	4.320×10^{-2}	8.315×10^{-2}	7.932×10^{-2}	2.089×10^{-4}
From EADL	8.787×10^{-1}	4.037×10^{-2}	7.920×10^{-2}	8.091×10^{-2}	5.312×10^{-4}
Chen *et al*	8.787×10^{-1}	4.037×10^{-2}	7.910×10^{-2}	8.091×10^{-2}	5.312×10^{-4}
Krause (1979) [42]	8.770×10^{-1}	4.100×10^{-2}	7.400×10^{-12}	7.400×10^{-2}	-
Yields	ω_{M_2}	ω_{M_3}	ω_{M_4}	ω_{M_5}	ω_{N_1}
This work	7.109×10^{-4}	5.783×10^{-4}	3.832×10^{-4}	3.218×10^{-4}	2.132×10^{-5}
From EADL	1.607×10^{-3}	1.679×10^{-3}	1.626×10^{-3}	1.500×10^{-3}	5.975×10^{-5}
Chen *et al*	1.607×10^{-3}	1.679×10^{-3}	1.627×10^{-3}	1.500×10^{-3}	5.975×10^{-5}
Yields	ω_{N_2}	ω_{N_3}	ω_{N_4}	ω_{N_5}	
This work	1.830×10^{-5}	2.400×10^{-5}	5.063×10^{-5}	2.687×10^{-11}	
From EADL	7.020×10^{-5}	2.055×10^{-5}	1.061×10^{-7}	1.243×10^{-7}	
Chen *et al*	7.020×10^{-5}	2.055×10^{-5}	1.061×10^{-7}	1.102×10^{-7}	

The calculated results shown for the MCDFGME radiative yields are in accordance with the correspondent values taken from EADL data tables for the K and L subshells. Nevertheless, for the M and N subshells the differences are higher, as expected. In Table 4.10 a more detailed comparison is made with the available literature.

The comparison of the K, L M and N fluorescent yields of ^{125}Te with some of the available literature and the EADL values shows that, for the L and M shells the differences are much higher than for the K shell, with the major relative diference values found for the M shell.

Table 4.10: ^{125}Te: Fluorescence yields for K, L, M and N shells.

Source	Fluorescent yields				Rel. Diff. MCDFGME-Source			
Yields	ω_{K}	ω_{L}	ω_{M}	ω_{N}	$\Delta\omega_K$ [%]	$\Delta\omega_L$ [%]	$\Delta\omega_M$ [%]	$\Delta\omega_N$ [%]
This work	8.874×10^{-1}	4.127×10^{-2}	2.357×10^{-4}	1.273×10^{-5}	-	-	-	-
From EADL	8.787×10^{-1}	4.246×10^{-2}	7.513×10^{-4}	1.939×10^{-5}	0.99	-2.80	-68.63	-34.35
Walters and Bhalla (1971) [43]	9.046×10^{-1}	-	-	-	-1.90	-	-	-
Bambynek *et al* (1972) [39]	8.750×10^{-1}	-	-	-	1.42	-	-	-
Krause (1979) [42]	8.770×10^{-1}	-	-	-	1.19	-	-	-
Chen *et al* (1983)	8.787×10^{-1}	-	-	-	0.99	-	-	-
Kostroun *et al*	8.900×10^{-1}	-	-	-	-0.29	-	-	-
Cohen (1987)	-	7.740×10^{-2}	-	-	-	-46.68	-	-
Hubbell (1989) [44]	8.750×10^{-1}	7.650×10^{-1}	2.980×10^{-3}	-	1.42	-46.05	-92.09	-
Hubbell *et al* (1994) [45]	8.830×10^{-1}	9.340×10^{-2}	-	-	0.50	-55.81	-	-
Puri *et al* [46]	-	8.600×10^{-2}	-	-	-	-52.01	-	-
Öz *et al* [47]	-	8.100×10^{-2}	-	-	-	-49.05	-	-
Bendjedi *et al* [48]	-	7.630×10^{-2}	-	-	-	-45.91	-	-

4.3 Monte Carlo Simulation of Auger Electron Spectra

The Auger Spectra were generated through the use of the MC cascade simulator code whose algorithm is decribed in Chaper 3 (3.3). To simulate the spectra 1.0^{9} cascades were generated using transition probabilities and electron energies calculated with MCDFGME code. The results are presented in Figure 4.13 and compared with existing EADL database values.

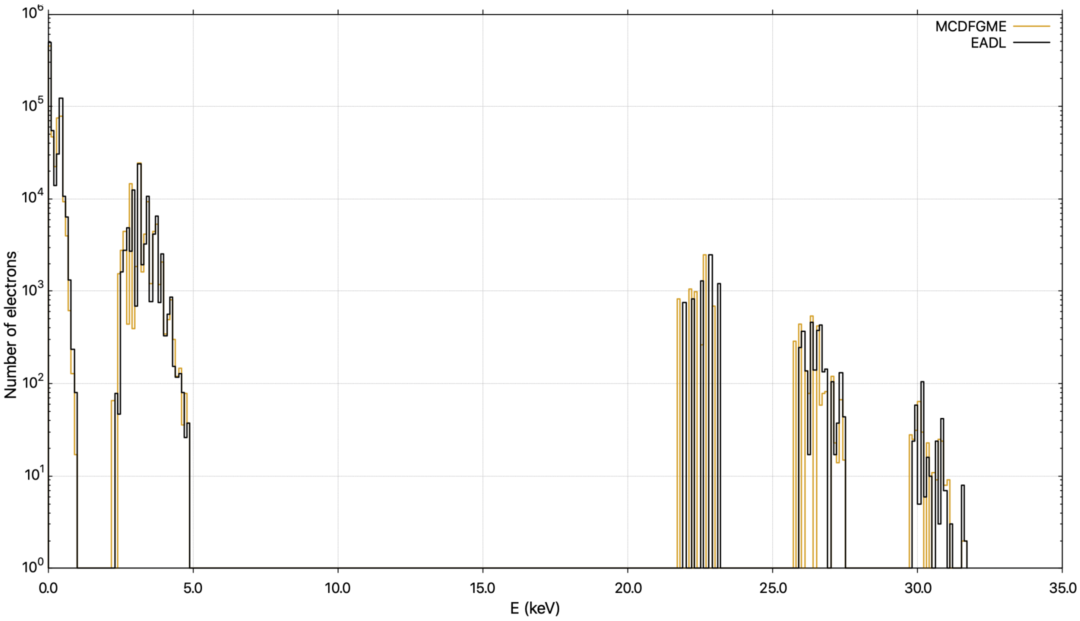

Figure 4.13: Auger spectra obtained for EADL and MCDFGME code calculated data. The number of electrons corresponds to the total number relative to the 1.0^{9} cascades.

According to the simulated spectra obtained for MCDFGME and EADL data, the majority of Auger electrons is emitted with energies lower than 5 keV in the process of the atomic relaxation of ^{125}Te. For the MCDFGME data, an average of 7 Auger electrons are emitted per decay; the total energy is of 77.29 keV. In the case of EADL data, the same number of Auger electrons are emitted but with a total energy of 82.90 keV.

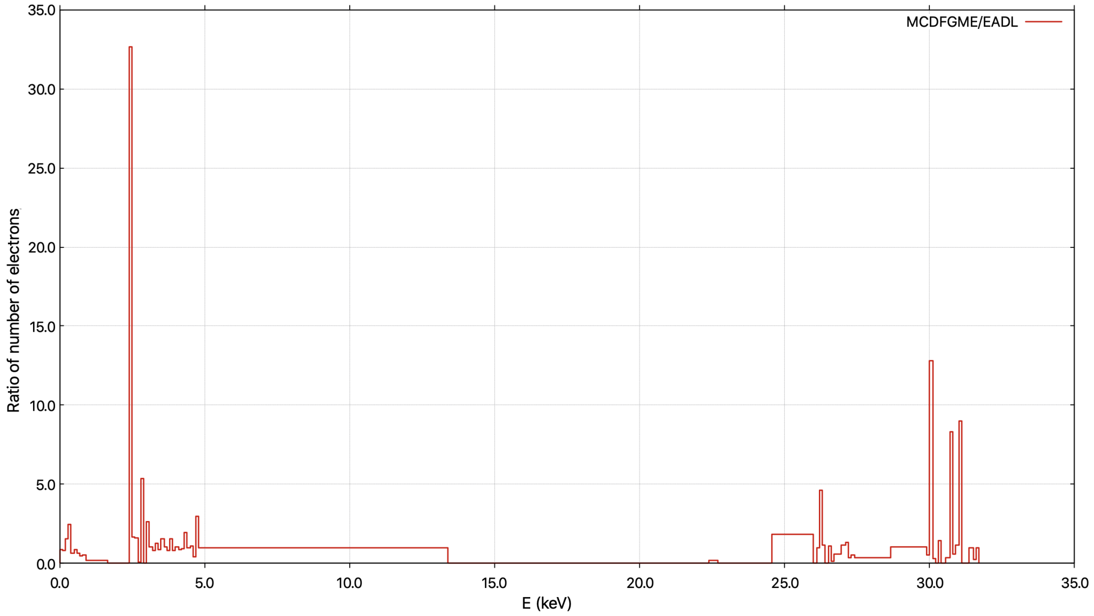

Figure 4.14: Ratio between Auger spectra obtained for EADL and MCDFGME code calculated data.

With regard to the comparison between MCDFGME and EADL showed in Figure 4.14, there are differences between those data across the Auger spectrum but more evident for energies lower than 5 keV and above 25 keV.

Chapter 5

Microdosimetric simulations

In this chapter, the virtual simple and modified MIRD model used to calculate the Auger electrons dose deposition in a cell through a Monte Carlo simulation with PENELOPE are described. The results of the S-values, radial dose distribution, Auger energy deposition spectra and Linear Energy Transfer are then presented and compared with some of the available literature.

5.1 MIRD model using PENELOPE

The interaction of particles with matter is, in essence, a stochastic process, so MC simulations represent an excellent approach for the transport of particles through different materials and the most reliable technique to estimate dose deposition in complex systems [49]. Microdosimetry of Auger electrons is performed inside small-scoring geometries. It is worth noting, however, that lack of experimental data for validation of MC simulations at microscale level implies the comparison of results with data derived from other Monte Carlo codes or semi-analytical methods as the one of Medical Internal Radiation Dose (MIRD), which is frequently employed as a standard for verification of simulations. In this way, the micro-dosimetry calculations for ^{40}K (^{40}Ar) and ^{125}I (^{125}Te) were performed using PENELOPE on an event-by-event Monte Carlo simulation and with the virtual phantom geometry based on the MIRD formalism, presented by the MIRD committee of the American Nuclear Society of Nuclear Medicine, back in 1997 [50].

MIRD model was formalized as semi-analytical method to provide dosimetric data at subcelular scale based on the fraction of energy released from the source, S, that is absorbed in the target zone, T. The S-value, $S(S \leftarrow T)$, which is specific to the radionuclide and the virtual phantom is defined as,

$$\frac{dD}{dt}(S \leftarrow T) = S(S \leftarrow T)A_S \tag{5.1}$$

where A_S is the activity in Bq of the radionuclide at the source site S in the cell and $dD/dt(S \leftarrow T)$ is the dose rate in Gy/s at the target T due to the source S; thus the S-value is expressed in Gy/(Bq s).

The PENELOPE code system simulates the coupled electron-photon transport in several materials from 50 eV to 1 GeV [19]. It includes the geometry package PENGEOM used to generate complex material systems.

Geometry of the virtual cell

To calculate, at microscale, the Auger electrons dose deposition in a cell, two spherical virtual cells were simulated: the first one with a cytoplasm and nucleus radii of 4 and 2 μm, respectively, and a chromosome of 0.7 μm; a second virtual spherical cell with a cytoplasm and nucleus of radii 6 μm and 5 μm, respectively, and with six spheres with radius of 0.7 μm located in different positions and representing the chromosomes. The virtual cells where defined according to MIRD formalism (modified, since in the case of the first virtual cell an additional small sphere was added representing a chromosome and, in the case of the second virtual cell, six chromosomes were added instead). The geometry of the virtual cells is illustrated in Figure 5.1 and Figure 5.2; For both cases the source was considered isotropic.

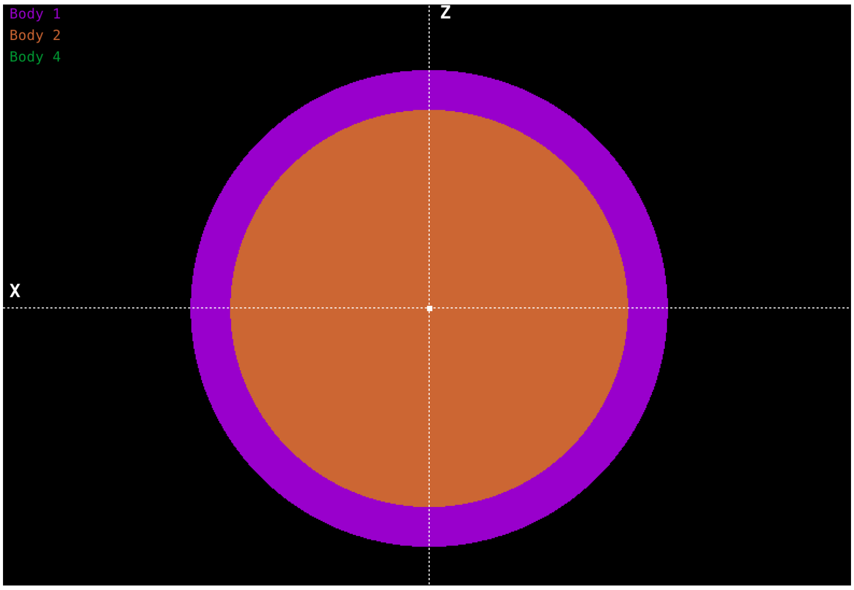

Figure 5.1: MIRD geometry (modified) used for MC simulation. Two shells were used, with the nucleus radius = 2 μm, cytoplasm radius= 4 μm and corresponding to bodies 2 and 1 respectively. An additional sphere with radius = 0.7 μm was centered and represents body 4.

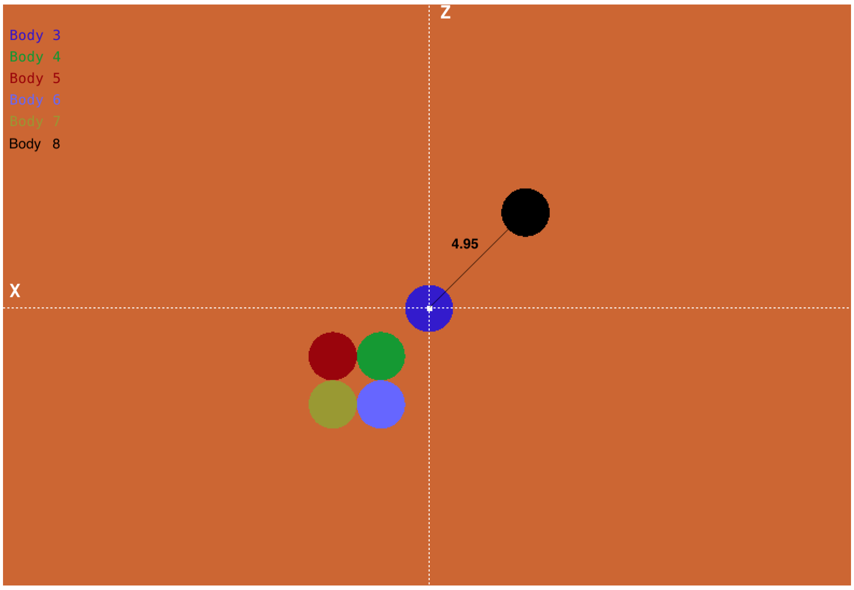

Figure 5.2: MIRD geometry (modified) used for MC simulation. Two shells were used, with the nucleus radius = 5 μm and cytoplasm radius= 6 μm and corresponding to bodies 1 and 2 respectively. Six additional spheres with radii 0.7 μm were placed inside the nucleus to represent several chromosomes. These six spheres correspond to bodies 3, 4, 5, 6, 7 and 8.

Event-by-event MC simulations require accurate cross-section data, which is essentially available for water. Since it is the main constituent of living organisms [51, 52], cell and nucleus were modeled with water density (1 g/cm^3).

5.2 Results for ^{125}I microdosimetric calculations

The geometry setups described in Section 5.1 were used to calculate the absorbed doses for two source distributions, refered as MIRD simple and MIRD modified (labeled as Sim$_{MIRD}$ and Mod$_{MIRD}$, respectively). For the sake of comparison, for both geometries the MC simulations were performed for MCDFGME and EADL data, so the absorbed dose in the nucleus of a cell could be compared and the impact of the differences between those data, in terms of atomic properties, analyzed for the dose deposition in the nucleus.

5.2.1 S-values for MIRD geometry: MCDFGME and EADL data

To calculate the S-values according to the MIRD formalism, the self-absorption was considered since the source was positioned inside the nucleus and, more specifically, at the center of the chromosome. The results are presented in Table 5.1.

The results of the S-values for the cytoplasm, nucleus and chromosome (correspondent to bodies 1, 2 and 3, respectively) are in accordance to what was expected and in agreement with the MIRD values and the ones from [53]. In the case of the nucleus structure, the differences are due to the fact that, in this work, the S-values have been calculated to the volume of the nucleus with the chromosome volume subtracted, and the chromosome corresponds to the strucure where most of the dose is aborbed. When compared with the sum of the $S - values$

Table 5.1: S-values for modified MIRD geometry considered: one cell (nucleus, cytoplasm and one chromosome) with the source positioned at the center of the chromosome. The MC statistical uncertainty is 0.003% for the entire calculation.

Scoring Volume	MCDFGME	EADL	Rel. Diff.
	S-value [Gy/(Bq.s)]	S-value [Gy/(Bq.s)]	ΔS-value [%]
Body 1 (Cytoplasm)	$(2.713 \pm 0.003) \times 10^{-4}$	$(2.056 \pm 0.003) \times 10^{-4}$	1.84
Body 2 (Nucleus-Chromosome)	$(1.018 \pm 0.001) \times 10^{-4}$	$(1.007 \pm 0.001) \times 10^{-4}$	1.11
Body 4 (Chromosome)	$(5.968 \pm 0.001) \times 10^{-2}$	$(5.764 \pm 0.001) \times 10^{-2}$	3.52

Table 5.2: Comparison of S-values for MIRD geometry considered. The MC statistical uncertainty is 0.003% for the entire calculation of MCDFGME and EADL data.

	S-values [Gy/(Bq.s)]			
Scoring Volume	MCDFGME	EADL	MIRD [53]	Di Maria *et al* [53]
Nucleus (Bodies 2+3)	5.978×10^{-2}	5.774×10^{-2}	4.850×10^{-2}	4.870×10^{-2}

for bodies 2 and 3 (Table 5.2), the relative difference between MCDFGME data and MIRD and Di Maria *et al* results is of 23,25% and 22.75%, respectively. For EADL data those differences are of 19.96% and 18.56%, respectively.

In terms of the comparison between MCDFGME and EADL data, the positive relative differences seem to suggest an underestimation of the dose deposited in the vicinity of the source when EADL data is used. In the case of the cytoplasm this difference is of 31.96%. With regard to the maximum dose absorbed in the cell, the difference between MCDFGME and EADL data is of 1.80%.

5.2.2 S-values for modified MIRD geometry: MCDFGME and EADL data

To study the impact of the source position and presence of several chromosomes on the dose absorbed in the cell, the modified MIRD geometry was adapted to contain 6 chromosomes. The results are presented in Tables 5.3 and 5.4.

Table 5.3: S-values for modified MIRD geometry considered: 6 chromosomes with the source positioned at the center of the nucleus (Body 3). The MC statistical uncertainty is 0.003%.

Scoring Volume	MCDFGME	EADL	Rel. Diff.
Chromosome	S-value [Gy/(Bq.s)]	S-value [Gy/(Bq.s)]	ΔS-value [%]
Body 1	$(9.128 \pm 0.001) \times 10^{-9}$	$(8.929 \pm 0.001) \times 10^{-9}$	2.20
Body 2	$(3.412 \pm 0.004) \times 10^{-8}$	$(3.345 \pm 0.004) \times 10^{-8}$	2.00
Body 3	$(5.968 \pm 0.001) \times 10^{-2}$	$(5.764 \pm 0.001) \times 10^{-2}$	3.56
Body 4	$(5.791 \pm 0.036) \times 10^{-5}$	$(5.715 \pm 0.035) \times 10^{-5}$	1.33
Body 5	$(2.842 \pm 0.027) \times 10^{-5}$	$(2.792 \pm 0.027) \times 10^{-5}$	1.81
Body 6	$(2.835 \pm 0.027) \times 10^{-5}$	$(2.789 \pm 0.027) \times 10^{-5}$	1.68
Body 7	$(2.071 \pm 0.023) \times 10^{-5}$	$(2.019 \pm 0.023) \times 10^{-5}$	2.56
Body 8	$(2.069 \pm 0.023) \times 10^{-5}$	$(2.020 \pm 0.023) \times 10^{-5}$	2.38

Table 5.4: S-values for modified MIRD geometry considered: 6 chromosomes with the source positioned at the center of Body 8. The MC statistical uncertainty is 0.003% for the entire calculation.

Scoring Volume	MCDFGME	EADL	Rel. Diff.
Chromosome	S-value [Gy/(Bq.s)]	S-value [Gy/(Bq.s)]	ΔS-value [%]
Body 1	$(8.679 \pm 0.001) \times 10^{-9}$	$(8.608 \pm 0.001) \times 10^{-9}$	0.80
Body 2	$(2.525 \pm 0.003) \times 10^{-8}$	$(2.489 \pm 0.003) \times 10^{-8}$	1.50
Body 3	$(2.106 \pm 0.025) \times 10^{-5}$	$(2.037 \pm 0.023) \times 10^{-5}$	3.32
Body 4	$(1.252 \pm 0.021) \times 10^{-5}$	$(1.217 \pm 0.020) \times 10^{-5}$	2.86
Body 5	$(8.930 \pm 0.190) \times 10^{-6}$	$(8.886 \pm 0.178) \times 10^{-6}$	0.48
Body 6	$(8.917 \pm 0.178) \times 10^{-6}$	$(8.868 \pm 0.178) \times 10^{-6}$	0.56
Body 7	$(6.198 \pm 0.156) \times 10^{-6}$	$(6.348 \pm 0.156) \times 10^{-6}$	-2.36
Body 8	$(5.968 \pm 0.001) \times 10^{-2}$	$(5.765 \pm 0.001) \times 10^{-2}$	3.52

According to the results presented for the S-values in the cases of cells with 6 chromosomes but with the source positioned in different locations, the values seem to suggest that, as expected, most of the dose is absorbed in the vicinity of the source. In the case where the source is positioned at the center of Body 8 (chromosome), a reduction of -25.98% in the S-value of the cytoplasm was verified.

5.2.3 Radial Dose distribution: MCDFGME and EADL data

The radial dose distribution for MCDFGME and EADL data was obtained from the results of the simulations with the Sim$_{MIRD}$ geometry described in Section 5.1. The source was placed at the center of the chromosome with radius 0.7 μm. The results are presented in Figure 5.3.

According to the results for the radial distribution of dose per decay of ^{125}I, the dose is mainly

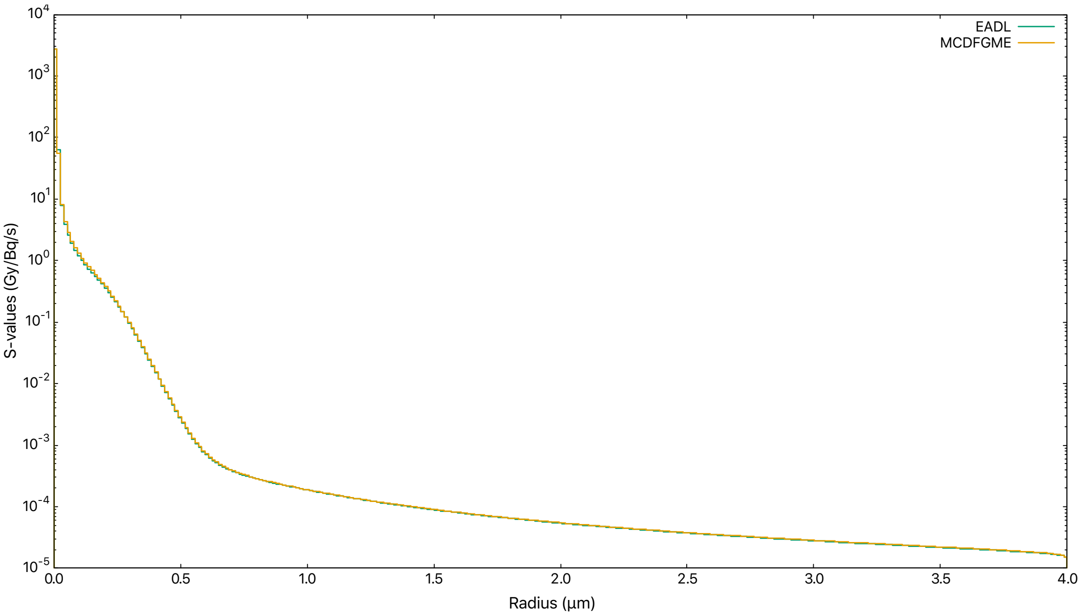

Figure 5.3: ^{125}Te: radial distribution of S-values for the Auger emission (MCDFGME and EADL data).

deposited in the vicinity of the source, mostly in a radius of 0.5 μm inside the chromosome where the ^{125}I source is placed.

With regard to the comparison between MCDFGME and EADL data, the differences emerge for the radii values in the range of the chromosome radius, with MCDFGME deposited doses per decay being higher than the EADL ones. This seems to suggest that EADL values might underestimate the deposited doses inside the chromosome and, in this way, close to DNA.

5.2.4 Auger energy deposition spectra: MCDFGME and EADL data

As with the radial dose distribution, the Auger energy deposition spectra for MCDFGME and EADL data was obtained from the results of the simulations with the Sim$_{MIRD}$ geometry described in Section 5.1. The source was placed at the center of the chromosome with radius 0.7 μm as well. The results are presented in Figure 5.4.

The results presented for the Auger deposition spectra are in accordance with what was expected: the smallest range of energies deposited is assigned to the chromosome but this sctrucure represents the one where Auger electrons energy is more likely to be deposited due their small range.

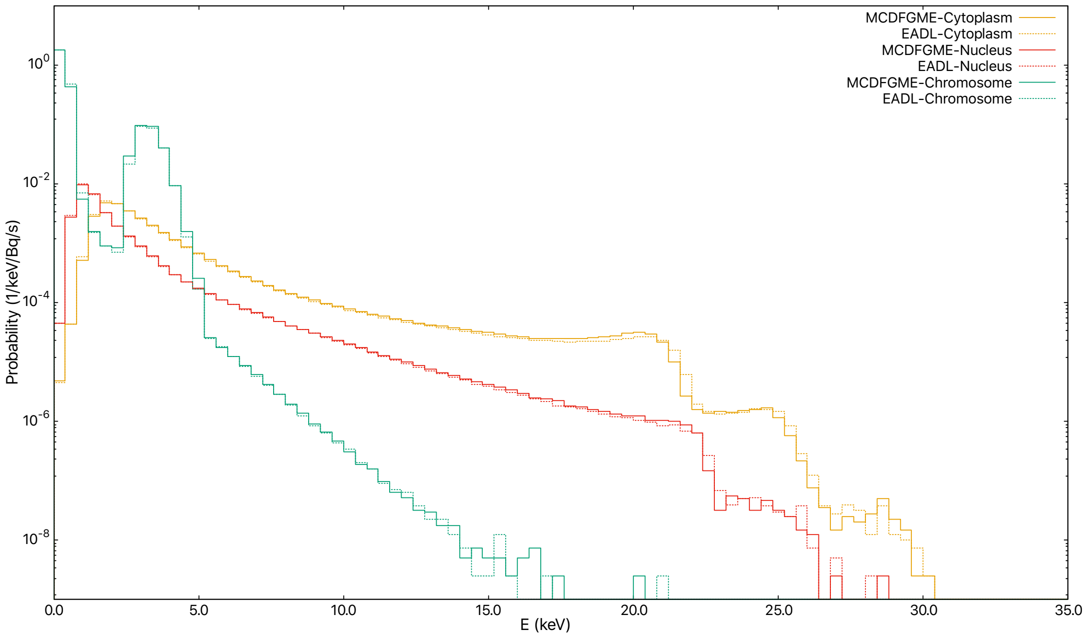

Figure 5.4: ^{125}Te: Auger energy deposition spectra per decay (MCDFGME and EADL data).

5.2.5 Linear Energy Transfer: MCDFGME and EADL data

As with the radial dose distribution and the Auger energy deposition spectra, the LET results were obtained for the simulations with the Sim$_{MIRD}$ geometry described in Section 5.1. The source was placed at the center of the chromosome with radius 0.7 μm as well. The results are presented in Figures 5.5 and 5.6.

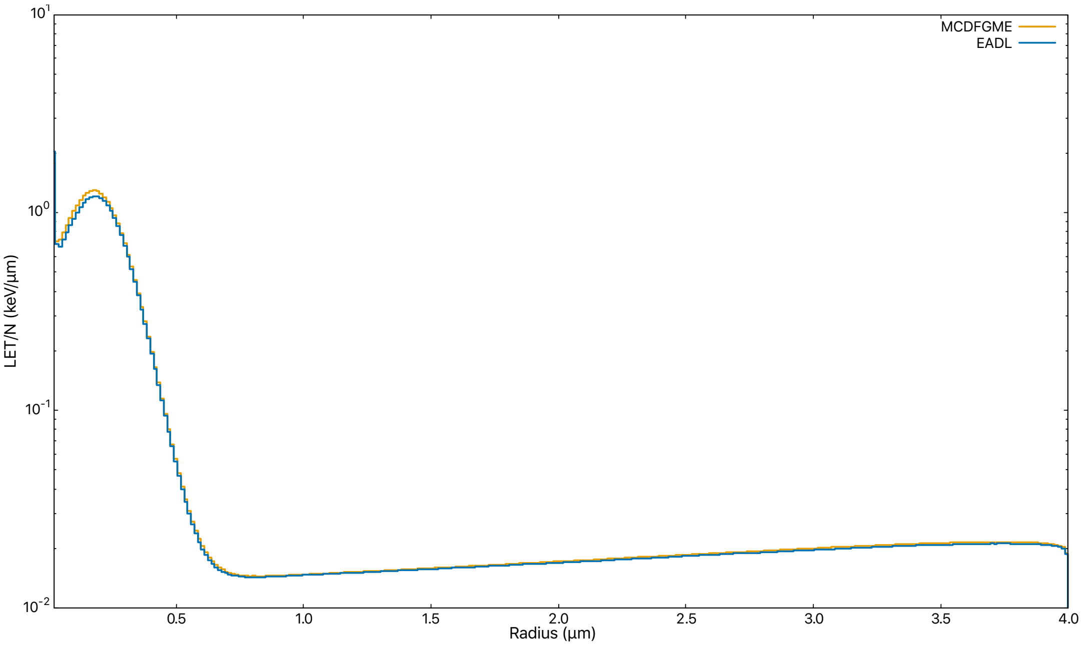

Figure 5.5: ^{125}Te: LET per decay for the Auger emission (MCDFGME and EADL data).

The results of the LET per decay for MCDFGME and EADL data show that the highest values of LET are determined within the chromosome. These values are in accordance to what was expected and with the results showed in Figure 5.3.

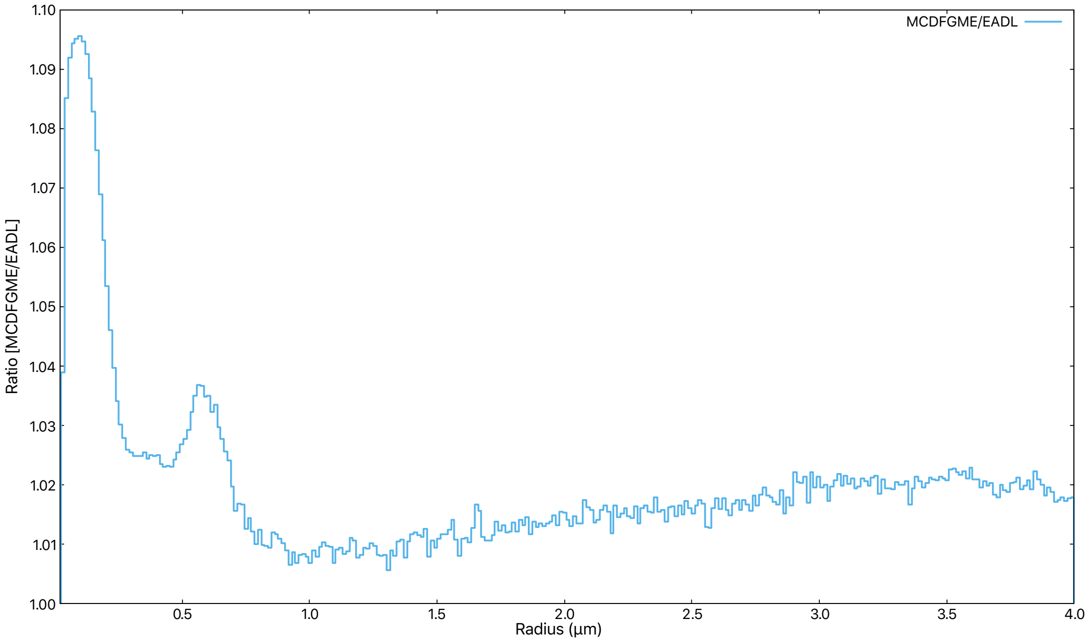

Figure 5.6: ^{125}Te: MCDFGME/EADL LET per decay ratio for the Auger emission.

In terms of the ratio between LET values of MCDFGME and EADL data, the values higher than 1.0 suggest that EADL data underestimates the LET within the cell. In the rage of radii lower than 1.0 μm these differences are higher in the vicinity of the source. Since for this simulation the source was placed at the center of the chromosome with radius 0.7 μm these results seem to indicate the highest differences between MCDFGME and EADL have more impact in the region close to DNA.

Chapter 6

Conclusions

This thesis describes the determination of Auger and radiative atomic transition probabilities and energies of the elements ^{40}Ar and ^{125}I using the Dirac-Fock method with the state of the art MCDFGME code, with the first element having been used to validate the methodology used to obtain those transition probabilities and energies according to the normalization method of the EADL data format. ^{125}I is frequently used for low dose brachytherapy treatments but, due to its Auger electrons emission, it is suitable to targeted radionuclide Auger therapy as well. The main feature of the Auger electrons to be used in cancer therapy is their short range, from nanometers to micrometers, that allows them to deposit most of their energy in the vicinity of the source and sparing normal tissues adjacent to the tumor. Together with the atomic transition probabilities and energy values, the simulation of the atomic cascade of the relaxation process that follows the ionization of an atom is necessary. Several processes may lead to this cascade, which is a stochastic process, and the emission of Auger electrons, be they the photoionization or the decay modes like electron capture or internal conversion. In the case of ^{125}I the Auger electrons are emitted as a consequence of the EC decay.

The Dirac-Fock method used, which was described in Chapter 2 and is the relativistic equivalent of the non-relativistic Hartree-Fock method, allows the calculation of approximate wavefunctions and energies of N-electron atomic systems using the *Slater determinants* that, combined in linear combinations form the CSF and enable the electronic correlation to be taken into account. Those CSF represent eigenstates of J^2 and J_z and their surperposition constitutes the total MCDF wavefunction. The MCDFGME code implements the full MCDF method, however, due to the fact of being very time consuming, in this work a mixing of electronic configurations with the same J and obtained from different jj couplings were used instead of mixing several configurations in the expansions of the CSF. The corrections applied to the relativistic hamiltonian of the system were two and of the radiative type: the vacuum polarization and self-energy.

The EADL tabulates atomic transition probabilities and energies of singly-ionized atoms in a specific type format, for which the normalized partial widths are used to describe the transition probabilities and the average energies to describe the transitions from a one-hole subshell to higher one-hole and two-hole subshells for the radiative and Auger transitions, respectively. In the same Chapter 3, a description of the MC code used to generate the Auger-electron spectra is presented. The cascade that makes part of the relaxation process that follows the ionization of an atom is a stochastic process, so the code used to perform the MC simulation takes as input the probabilities for vacancies to be created in K, L an M shells and random number generators for the selection of the transition according to the calculated transition probabilities for each subshell.

In Chapter 4 the results for the atomic transitions of ^{40}Ar and ^{125}I were presented. In the case of ^{40}Ar, highest differences between MCDFGME results and EADL tabulated data for the Auger transition probabilities were found for the L shell, on a per shell basis, and for the more external transitions L_2-M_2M_2 with a ratio between MCDFGME and EADL values of ~6.8. In the case of the radiative transitions probabilities of ^{40}Ar, the highest difference between MCDFGME and EADL data was found for the internal L_1 initial vacancy. For the atomic shell widths the major differences were for the L_2 and L_3 initial vacancies and with the MCDFGME values lower than the EADL ones; this difference must be due to the fact that, for EADL tables, no data is available for transitions with vacancies originated in the M shell, so the correspondent widths of the L subshells were overestimated. For the K shell the MCDFGME values are ~7.5% higher. In terms of Auger yields, the relative differences between MCDFGME and EADL data is small, with values of 0.16% and 0.05% for the K and L shells respectively.

In the case of ^{125}I, the differences between MCDFGME and EADL data with regard to Auger transition probabilities are more relevant, with ratios close or higher than 100 for the external M and N shells, in accordance to what was expected. For the radiative transitions the ratios are smaller but in the order of 10 for the external N shells. With regard to the atomic shell widths, the highest differences between MCDFGME and EADL data were found for the N subshells, with values higher than 500%. As with ^{40}Ar, the results for the external subshells seem to suggest an overestimation of the EADL data for these subshells and due to the fact that, for O shells, no data is available on EADL tables. What concerns the Auger and Radiative yields, for the Auger ones the differences on a subshell basis are small, but on a shell basis the highest differences were found for the K and N shells, with values of -7.26% and -5.45%, respectively; for the radiative yields the differences are much higher, with values of ~ -68.8% and ~ -34.4% for the M and N shells, respectively.

The Auger spectra generated through the MC cascade simulator code and using the the transition probabilities and energies calculated with MCDFGME code was compared with the one obtained using the correspondent transition probabilities and energies taken from EADL tables. In spite of the differences found across the whole spectrum, when comparing both the differences are more evident for energies higher than 10 keV.

In Chapter 5 the results of the microdosimetry simulations with PENELOPE were presented in terms of the calculated S-values, radial dose deposition, Auger energy deposition spectra, LET per decay and ratio between the LET values derived from MCDFGME data and the ones from EADL tables. In terms of S-values, the major differences between MCDFGME and EADL data occur within the chromosomes when the source is positioned at its center. With regard to the Auger energy deposition spectra, the highest probability of energy deposition arises for the chromosome in the case of the simple MIRD geometry, which is in accordance with what expected due to the very low range of Auger electrons. When comparing MCDFGME and EADL data in terms of the LET, the differences are of about 10% within radius values of 0.7 μm, which corresponds to the chromosome radii. One more time, these results corroborate the predictions on the discrepancies between EADL data and the updated values calculated with MCDFGME code.

6.1 Prospects for future work

6.1.1 Calculations of atomic parameters

Due to the fact of being very time consuming, the full MCDF method was not used in the calculations performed. Instead, mixing electronic configurations with the same J and obtained from different jj couplings were used. Nevertheless, the electronic correlation taken into account when using the multiconfiguration method may be significant in the calculation of outer subshell transition probabilities, where the high LET Auger electrons originate. In this way, the first possible work to develop would be to use the full MCDF mode for ^{125}I. In spite of not being considered as a heavy-element, due to the importance of high LET electrons for Auger therapy, the implementation of the full MCDF method could give rise to more accurate results for the transition probabilities of outer subshells.

In Chapter 3 the shake-off and shake-up processes were briefly mentioned. These effects result from sudden changes in the central potential after the removal of an electron by photoionization, IC, EC or radiative/non-radiative transitions. Those changes can lead to excitation of an atomic electron into a lesser-bound excited state or into the continuum. Due to those effects, the atom can be double or even triple ionized and causing changes in the calculated transition probabilities. In this way, a second prospect for a future work would be to consider the shake-off and shake-up effects when simulating the vacancy cascade that originates from the ionization of the atom.

It would also be desirable to use the MCDF method to update the transition probabilities in other promising atomic systems for targeted therapy with Auger emitters. An example is the case of ^{177}Lu which decays to ^{177}Hf by β-emission.

6.1.2 Microdosimetric simulations

The results of the microdosimetric simulations of this work suggest the Auger electrons deposit most of their energy in the vicinity of the ^{125}I source, within a range of 0.5 μm. Corresponding to the region with the highest LET values, the Auger electrons that deposit there their energy correspond to the ones involved in the outer subshell transitions. From the results of the energy deposition spectra, the highest probability is assigned to very low energies, in the range of $\sim$5 eV. Despite of tracking the electrons in an event-by-event mode, the cross sections databases of PENELOPE cover only the energy interval in the range of 50 eV up to 1 GeV, which may represent a limitation in the accuracy of microdosimetric simulations. Platforms like Geant4-DNA [54] may represent good improvements in the accuracy of these simulations, since this toolkit provides much lower energy thresholds of $\sim$7 eV. Furthermore it also includes extension to perform simulation of the chemical reactions that follow the physical energy deposition and ionization stages. In this way, a third prospect for a future work would be to perform the simulations of simple and modified MIRD geometries using this platform instead of PENELOPE and compare the results with the ones present in this work.

Bibliography

[1] P. Auger. The auger effect. *Surf Sci*, 48(1):1–8, 1975. ISSN 0039-6028. doi: https://doi.org/10.1016/0039-6028(75)90306-4.

[2] S. T. Perkins, M. H. Chen, D. E. Cullen, and J. H. Hubbell. *Tables and graphs of atomic subshell and relaxation data derived from the LLNL Evaluated Atomic Data Library (EADL), $\mathbf{Z}$=1-100*. Lawrence Livermore Nat. Lab., Livermore, CA, 1991.

[3] J. H. Scofield. Radiative Decay Rates of Vacancies in the $\mathbf{K}$ and $\mathbf{L}$ Shells. *Phys Rev*, 179 (1):9–16, 1969. doi: 10.1103/physrev.179.9.

[4] J. H. Scofield. Relativistic Hartree-Slater values for $\mathbf{K}$ and $\mathbf{L}$ X-ray emission rates. *Atom Data Nucl Data*, 14(2):121–137, 1974. doi: 10.1016/s0092-640x(74)80019-7.

[5] J.H. Scofield. Radiative Transitions. In *Atomic Inner-Shell Processes*, pages 265–292. Elsevier, 1975. doi: 10.1016/b978-0-12-196901-1.50012-1.

[6] M. H. Chen, B. Crasemann, and H. Mark. Relativistic radiationless transition probabilities for atomic $\mathbf{K}$ and $\mathbf{L}$ shells. *Atom Data Nucl Data*, 24(1):13–37, 1979. doi: 10.1016/0092-640x(79)90037-8.

[7] M. H. Chen, E. Laiman, B. Crasemann, M. Aoyagi, and H. Mark. Relativistic $\mathbf{L}$-shell Auger and Coster-Kronig rates and fluorescence yields. *Phys Rev A*, 19(6):2253–2259, 1979. doi: 10.1103/physreva.19.2253.

[8] M. H. Chen, B. Crasemann, and H. Mark. Relativistic $\mathbf{M}$-shell radiationless transitions. *Phys Rev A*, 21(2):449–453, 1980. doi: 10.1103/physreva.21.449.

[9] M. H. Chen, B. Crasemann, and H. Mark. Widths and fluorescence yields of atomic $\mathbf{L}$-shell vacancy states. *Phys Rev A*, 24(1):177–182, 1981. doi: 10.1103/physreva.24.177.

[10] M. H. Chen, B. Crasemann, and H. Mark. Radiationless transitions to atomic $\mathbf{M_{1,2,3}}$ shells: Results of relativistic theory. *Phys Rev A*, 27(6):2989–2994, 1983. doi: 10.1103/physreva.27.2989.

[11] B. Q. Lee. *A Numerical Model of Atomic Relaxation and its Applications*. PhD thesis, Department of Nuclear Physics, Research School of Physics and Engineering, The Australian National University, 2017.

[12] P. Saracco M. G. Pia and M. Sudhakar. Validation of $\mathbf{K}$ and $\mathbf{L}$ shell radiative transition probability calculations. *IEEE T Nucl Sci*, 56(6):3650–3661, 2009. doi: 10.1109/tns.2009.2033793.

[13] M. Iliaš, V. Kellö, and M. Urban. Relativistic effects in atomic and molecular properties. *Acta Phys Slovaca*, 60(3), 2010. doi: 10.2478/v10155-010-0003-1.

[14] J. P. Desclaux. Relativistic Dirac-Fock expectation values for atoms with $\mathbf{Z} = 1$ to $\mathbf{Z} = 120$. *Atom Data Nucl Data*, 12(4):311–406, 1973. doi: 10.1016/0092-640x(73)90020-x.

[15] P. Indelicato and J. P. Desclaux. Multiconfiguration Dirac-Fock calculations of transition energies with QED corrections in three-electron ions. *Phys Rev A*, 42(9):5139–5149, 1990. doi: 10.1103/physreva.42.5139.

[16] Y. K. Kim, J. P. Desclaux, and P. Indelicato. Calculation of transition probabilities using the multiconfiguration Dirac-Fock method. *J Korean Phys Soc*, 33:218–222, 1998.

[17] B. Q. Lee, T. Kibédi, A. E. Stuchbery, and K. A. Robertson. Atomic Radiations in the Decay of Medical Radioisotopes: A Physics Perspective. *Comput Math Method M*, 2012:1–14, 2012. doi: 10.1155/2012/651475.

[18] MCDFGME code. Available at `http://dirac.spectro.jussieu.fr/mcdf/mcdf_welcome/mcdf_homepage.html`. Last updated on: 2005-08-09.

[19] *PENELOPE, A Code System for Monte Carlo Simulation of Electron and Photon Transport, Proceedings of a Workshop/Training Course*, 2001. OECD/NEA 5-7 November 2001 NEA/NSC/DOC(2001)19. ISBN:92-64-18475-9.

[20] A. I. Kassis. Therapeutic Radionuclides: Biophysical and Radiobiologic Principles. *Semin Nucl Med*, 38(5):358–366, 2008. doi: 10.1053/j.semnuclmed.2008.05.002.

[21] S. Aghevlian, A. J. Boyle, and R. M. Reilly. Radioimmunotherapy of cancer with high linear energy transfer (LET) radiation delivered by radionuclides emitting α-particles or Auger electrons. *Adv Drug Deliver Rev*, 109:102–118, 2017. doi: 10.1016/j.addr.2015.12.003.

[22] A. I. Kassis. The amazing world of auger electrons. *Int J Radiat Biol*, 80(11-12):789–803, 2004. doi: 10.1080/09553000400017663.

[23] S. B. Schwarz, N. Thon, K. Nikolajek, M. Niyazi, Joerg-Christian Tonn, Claus Belka, and Friedrich-Wilhelm Kreth. Iodine-125 brachytherapy for brain tumours - a review. *Radiat Oncol*, 7(1):30, 2012. doi: 10.1186/1748-717x-7-30.

[24] S. J. Adelstein, A. I. Kassisa, L. Bodei, and G. Mariani. Radiotoxicity of Iodine-125 and Other Auger-Electron-Emitting Radionuclides: Background to Therapy. *Cancer Biother Radio*, 18(3):301–316, 2003. doi: 10.1089/108497803322285062.

[25] National nuclear data center-NNDC. Available at `https://www.nndc.bnl.gov/nudat2/chartNuc.jsp`.

[26] M.J. Esteban and E. Séré. Nonrelativistic Limit of the Dirac-Fock Equations. *Ann Henri Poincare*, 2(5):941–961, 2001. doi: 10.1007/s00023-001-8600-7.

[27] D. R. Hartree. The Wave Mechanics of an Atom with a Non-Coulomb Central Field. Part I. Theory and Methods. *Math Proc Cambridge*, 24(01):89, 1928. doi: 10.1017/s0305004100011919.

[28] Y-K. Kim. Strengths and weaknesses of relativistic atomic structure calculations. *Phys Scripta*, T73:19–24, 1997. doi: 10.1088/0031-8949/1997/t73/001.

[29] C. B. Casteleiro. Transições radiativas e não-radiativas em átomos. cálculo dos rendimentos de fluorescência da camada $\mathbf{K}$ no Zn, Cd e Hg. Master's thesis, Departmento de Física, Faculdade de Ciências, Universidade de Lisboa, 2008.

[30] W. R. Johnson and G. Soff. The lamb shift in hydrogen-like atoms, $1 \leqslant \mathbf{Z} \leqslant 110$. *Atom Data Nucl Data*, 33(3):405–446, 1985. doi: 10.1016/0092-640x(85)90010-5.

[31] *The Theory of Auger Transitions*. Elsevier, 1976. doi: 10.1016/b978-0-12-169850-8.x5001-0.

[32] M. M. Bé, V. Chisté, C. Dulieu, E. Browne, V. Chechev, N. Kuzmenko, R. Helmer, A. Nichols, E. Schönfeld, and R. Dersch.

[33] R. Jenkins, R. Manne, R. Robin, and C. Senemaud. IUPAC—nomenclature system for X-ray spectroscopy. *X-ray Spectrom*, 20(3):149–155, 1991. doi: 10.1002/xrs.1300200308.

[34] M. O. Krause. Rearrangement of Inner Shell Ionized Atoms. *J Phys Colloq*, 32(C4):C4–67–C4–75, 1971. doi: 10.1051/jphyscol:1971415.

[35] L. Partanent. *Auger Cascade Processes in Xenon and Krypton Studied by Electron and Ion Spectroscopy*. PhD thesis, University of Oulu, 2007.

[36] T. A. Carlson. The Nature of Secondary Electrons Created as the Result of Electron Shake-Off and Vacancy Cascades. *Radiat Res*, 64(1):53, 1975. doi: 10.2307/3574168.

[37] J. Katakura. Nuclear data sheets for $\mathbf{A}$ = 125. *Nucl Data Sheets*, 112(3):495–705, 2011. doi: 10.1016/j.nds.2011.02.001.

[38] P. Persson, S. Lunell, A. Szoeke, B. Ziaja, and J. Hajdu. Shake-up and shake-off excitations with associated electron losses in X-ray studies of proteins. 2001.

[39] W. Bambynek, B. Crasemann, R. W. Fink, H. U. Freund, H. Mark, C. D. Swift, R. E. Price, and P. V. Rao. X-ray Fluorescence Yields, Auger, and Coster-Kronig Transition Probabilities. *Rev Mod Phys*, 44(4):716–813, 1972. doi: 10.1103/revmodphys.44.716. URL `https://doi.org/10.1103/revmodphys.44.716`.

[40] E. J. McGuire. K-Shell Auger Transition Rates and Fluorescence Yields for Elements Ar-Xe. *Phys Rev A*, 2(2):273–278, 1970. doi: 10.1103/physreva.2.273. URL `https://doi.org/10.1103/physreva.2.273`.

[41] V. O. Kostroun, M. H. Chen, and B. Crasemann. Atomic Radiation Transition Probabilities to the 1s State and Theoretical $\mathbf{K}$-Shell Fluorescence Yields. *Phys Rev A*, 3(2):533–545, 1971. doi: 10.1103/physreva.3.533. URL `https://doi.org/10.1103/physreva.3.533`.

[42] M. O. Krause. Atomic radiative and radiationless yields for $\mathbf{K}$ and $\mathbf{L}$ shells. *J Phys Chem Ref Data*, 8(2):307–327, 1979. doi: 10.1063/1.555594. URL `https://doi.org/10.1063/1.555594`.

[43] D. L. Walters and C. P. Bhalla. Nonrelativistic Auger Rates, X-ray Rates, and Fluorescence

Yields for the $\mathbf{K}$ Shell. *Phys Rev A*, 3(6):1919–1927, 1971. doi: 10.1103/physreva.3.1919. URL `https://doi.org/10.1103/physreva.3.1919`.

[44] J. H. Hubbell. *Bibliography and Current Status of K, L, and Higher Shell Fluorescence Yields for Computations of Photon Energy-Absorption Coefficients (Classic Reprint)*. Forgotten Books, 2018. ISBN 0366847449.

[45] J. H. Hubbell, P. N. Trehan, N. Singh, B. Chand, D. Mehta, M. L. Garg, R. R. Garg, S. Singh, and S. Puri. A Review, Bibliography, and Tabulation of $\mathbf{K}$, $\mathbf{L}$, and Higher Atomic Shell X-ray Fluorescence Yields. *J Phys Chem Ref Data*, 23(2):339–364, 1994. doi: 10.1063/1.555955. URL `https://doi.org/10.1063/1.555955`.

[46] S. Puri, D. Mehta, B. Chand, N. Singh, and P. N. Trehan. $\mathbf{L}$ shell fluorescence yields and coster—kronig transition probabilities for the elements with 25 $\leq \mathbf{Z} \leq$ 96. *X-ray Spectrom*, 22(5):358–361, 1993. doi: 10.1002/xrs.1300220507. URL `https://doi.org/10.1002/xrs.1300220507`.

[47] E. Öz, H. Erdoğan, and M. Ertuğrul. Calculation of average $\mathbf{L}$ shell fluorescence yields for the elements with 25 $\leq \mathbf{Z} \leq$ 101. *J Radioanal Nucl Ch*, 242(1):219–224, 1999. doi: 10.1007/bf02345924. URL `https://doi.org/10.1007/bf02345924`.

[48] A. Bendjedi, B. Deghfel, A. Kahoul, I. Derradj, F. Khalfallah, Y. Sahnoune, A. Bentabet, and M. Nekkab. $\mathbf{L}$ shell fluorescence yields and total ionization and X-ray production cross sections for elements with 40 $\leq \mathbf{Z} \leq$ 92. *Radiat Phys Chem*, 117:128–134, 2015. doi: 10.1016/j.radphyschem.2015.08.008. URL `https://doi.org/10.1016/j.radphyschem.2015.08.008`.

[49] D. W. O. Rogers. Fifty years of Monte Carlo simulations for medical physics. *Phys Med Biol*, 51(13):R287–R301, 2006. doi: 10.1088/0031-9155/51/13/r17.

[50] T. F. Budinger and S. M. Goddu. *MIRD cellular $\mathbf{S}$-values : self-absorbed dose per unit cumulated activity for selected radionuclides and monoenergetic electron and alpha particle emitters incorporated into different cell compartments*. Reston, Va. : Society of Nuclear Medicine, 1997. ISBN 0932004466. Includes bibliographical references and index.

[51] S. Uehara, H. Nikjoo, and D. T. Goodhead. Comparison and Assessment of Electron Cross Sections for Monte Carlo Track Structure Codes. *Radiat Res*, 152(2):202, 1999. doi: 10.2307/3580095.

[52] S. Incerti, A. Ivanchenko, M. Karamitros, A. Mantero, P. Moretto, H. N. Tran, B. Mascialino, C. Champion, V. N. Ivanchenko, M. A. Bernal, Z. Francis, C. Villagrasa, G. Baldacchino, P. Guèye, R. Capra, P. Nieminen, and C. Zacharatou. Comparison of GEANT4 very low energy cross section models with experimental data in water. *Med Phys*, 37(9):4692–4708, 2010. doi: 10.1118/1.3476457.

[53] S. Di Maria, A. Belchior, Y. Romanets, A. Paulo, and P. Vaz. Monte Carlo dose distribution calculation at nuclear level for Auger-emitting radionuclide energies. *Appl Radiat Isotopes*, 135:72–77, 2018. doi: 10.1016/j.apradiso.2018.01.013. URL `https://doi.org/10.1016/j.apradiso.2018.01.013`.

[54] Geant4-DNA. Available at `http://geant4-dna.org`. Last release on May 2020.